이학박사 학위논문

Development of Geometric Uncertainty Assessment System for Precise Radiotherapy

정밀 방사선치료를 위한 기하학적 불확실성 평가 시스템의 개발

2016년 8월

서울대학교 대학원

방사선응용생명과학 협동과정

김 휘 영

A Thesis of the Degree of Doctor of Philosophy

Development of Geometric Uncertainty Assessment System for Precise Radiotherapy

정밀 방사선치료를 위한 기하학적 불확실성 평가 시스템의 개발

August 2016

Interdisciplinary Program in Radiation Applied Life Science,
The Graduate School of Seoul National University
Hwiyoung Kim

ABSTRACT

Development of Geometric uncertainty Assessment System for Precise Radiotherapy

Hwiyoung Kim

Interdisciplinary Program in Radiation Applied Life Science

The Graduate School

Seoul National University

During the radiotherapy, the precise delivery of a planned beam may be hindered by geometrical uncertainties of machine related errors and patient related errors. Those geometrical uncertainties can make the treatment beam miss the target volume and accidentally hit the healthy organs. Hence, consequently, the target volume receive less dose than therapeutic dose. Thus this results in lower tumor control and higher complication probability.

The purpose of this dissertation is to develop two individual systems to assess those geometric uncertainties. First, in order to assess machine related errors, a

smartphone application for mechanical quality assurance (QA) of medical linear accelerators (LINAC) was developed. Second, in order to assess patient related motion errors, optical image-based motion tracking system using a stereo camera was developed. These systems were adopted to the clinic to test clinical feasibility following the accuracy and precision evaluation tests for each system.

The geometric uncertainty assessment systems we developed can be used for the mechanical QA of medical accelerators and the evaluation of patient's motion with proven accuracy and precision. Thus these systems have a strong potential of application in the clinic to provide precise radiotherapy by assessing geometrical uncertainties.

Keywords: Radiation Therapy, Geometric Uncertainty, Quality Assurance, Inter-fractional Error, Intra-fractional Error

Student Number: 2010-21892

List of Tables

TABLE 1. SYSTEM accuracy and precision: mean absolute errors and standard deviations of measured rotation angles (top) and lengths (bottom) for ten test sets. The other sources of error such as gantry sag were excluded. 40

TABLE 2. Comparison between the AutoMQA and manual results for the assessment of some mechanical QA items recommended by AAPM TG-142. We derived MAEs of measurements and measured total time taken by each method. 43

TABLE 3. Jaw position measurement result for standard setup (SSD = 100 cm, FS = 10×10cm2). Measured lengths were derived from the image length on the acquired image multiplied by calibration factor and averaged over total ten test results. 45

TABLE 4. Independent jaw position measurement result for the tests applied various intentional error. The intended errors were noted as (X jaw displacement, Y jaw displacement). 46

TABLE 5. Optimal parameter verification test: The differences for each case were discrepancies between measured field size and desired field size. 47

TABLE 6. Mechanical QA items (TG-142) list identifying availability with

AutoMQA system. 50

TABLE 7. The test sets with known translations. 71

TABLE 8. SYSTEM consistency: mean absolute errors of detected displacements of the IR markers with various brightness and contrast condition in each direction. 80

TABLE 9. The comparison of inter-fractional motions derived from the CBCT and the ROIM system. For patient 3 and 5, we acquired two orthogonal OBI images instead of CBCT images due to the large couch shift (thus rotational motions couldn't be assessed). 83

TABLE 10. Interfractional errors of each structures observed by ROIM system. 90

List of Figures

Figure 1. The aim of the radiotherapy is to maximize the tumor dose and to minimize normal tissue dose simultaneously thus improve tumor control probability and reduce complications. High dose region is fit to the target volume. 4

Figure 2. The geometric uncertainties related to machine errors. Machine related errors are due to deviations of mechanical properties of LINAC from the desired value. High-precision radiotherapy can be successful only if geometrical consistencies of the mechanical properties of LINAC such as gantry rotation angle and each jaw positions are insured to a high degree. 5

Figure 3. The geometric uncertainties related to the patient localization error. Patient set-up variation is due to errors in the daily positioning of the patient at each treatment fraction and it is called as inter-fractional error. Organ motion is the target volume displacement with respect to the treatment iso-center during a single fraction and this type of error is called as intra-fractional error. To assess those errors, internal margin and set-up margin is applied to the internal target volume and planning target volume, respectively. 6

Figure 4. An overview of the developed geometric uncertainty assessment system for radiotherapy. First, in order to assess machine related errors, a smartphone application for mechanical QA of LINAC is developed. Second, in order to assess patient related motion errors, optical image-based guidance

system using a stereo camera is developed. These systems were adopted to the clinic to test clinical feasibility. 7

Figure 5. A schematic of the AutoMQA system. The system is consisted of two main modules. The one is the motion sensor signal processing module which is for the gantry and the collimator rotation angle measurements by using various motion sensors embedded in a smartphone. The other is the optical image processing module which is for the jaw position, crosshair position, and SSD measurements by using high-resolution camera embedded in a smartphone. 16

Figure 6. A smartphone attached to the LINAC gantry, and the roll rotation axis of the smartphone is perpendicular to the central axis (CAX) of the medical accelerator. In order to control and receive the measured data from the device attached to the gantry, wireless communication module was implemented to make connection between another smartphone and the device via wireless network, specifically, Bluetooth®. 17

Figure 7. A process of sensor fusion method. The relative orientation of a smartphone is determined by a gyroscope primarily which measures angular velocity. Thereafter, relative orientation is corrected by an accelerometer or a compass to derive absolute orientation of a smartphone. The noises of signals from the accelerometer and the compass were removed by low-pass filters. 22

Figure 8. The process of the image preprocessing module. Light field and a cross-hair were recognized by the Canny method using a gray-scale image taken by the high-resolution camera. Then feature points were detected by the Harris method to calculate the locations of each of the jaws and the cross-hair. 24

Figure 9. A screen shot example of length calibration. The calibration factor was caclualted with the radius determined by detecting a circle (known geometry, for this example, 100 KRW) by using Hough transform algorithm. 26

Figure 10. An evaluation of the AutoMQA system accuracy. Motion sensor signal accuracy was evaluated by measuring orientation of the smartphone attached to the optical rotation stage and compared with the actual angle indicated by the optical stage (left). Image processing accuracy was evaluated by measuring template sizes of ten test sets at the source to surface distance of 100 cm following the calibration procedure with a 5 cm radius circle template (right). 30

Figure 11. The AutoMQA system can track the real-time position of crosshair with video mode, thus maximum deviation from the initial position of the crosshair (crosshair location at collimator angle of 0°) can be measured. 36

Figure 12. The mathematical relationship between real geometry and one projected on the image plane to derive camera-to-surface distance (CSD). ...37

Figure 13. A gantry rotation angle was assessed with the AutoMQA system and showed proven accuracy. AutoMQA system showed consistent result with the bubble level. 44

Figure 14. A schematic of the developed ROIM system. Three IR markers were attached on the skin of the patient. Reference positions of markers were calculated by RTPS and real-time positions of the markers with respect to iso-center of treatment room were calculated by stereo camera system installed on the inferior wall of treatment room. Then the positions of three IR reflector markers were registered with respect to the reference coordinate. The derived positional error was compared with that derived from the X-ray images (CBCT). 60

Figure 15. The stereo camera system mounted on the inferior wall of treatment room. The CCD cameras with IR filters receive the IR signals from the IR LEDs and interfaced to a PC. A railed frame was fabricated to accurately adjust the baseline between the two cameras. 62

Figure 16. A flow diagram of image processing for IR marker detection: raw IR markers image (top left), binary image with a threshold (top right), detected edges of the markers by the Canny method (bottom right), determined the

centroid of each edge (bottom left). 66

Figure 17. Three markers were attached to the template on the optical translation stage. 70

Figure 18. A description of clinical application of ROIM system. Each interfractional and intrafractional errors was derived from ROIM system and CBCT scans. Comparison between the calculated 6-DOF displacement from ROIM system and the estimated motion from CBCT scans were done. 77

Figure 19. Screen shots of ROIM system. The derived positional deviations were displayed in real-time. 78

Figure 20. An example of daily CBCT-reference planning CT registration results. Initial setup shows severe discrepancy of surface and soft tissue matching between two images. When rotation correction was applied, two images were matched better than the case with only translation correction was applied. 84

Figure 21. A trend graph and 3D distribution plot of the interfractional error for Lt. inner thigh patient. 85

Figure 22. A trend graph and 3D distribution plot of the interfractional error for

Lt. knee patient. 86

Figure 23. The measured intrafractional motion of Lt inner thigh patient for five fractions. The orange colored horizontal line represents the intrafractional motion estimated from the pre- and post-treatment CBCT images. 88

Figure 24. The measured intrafractional motion of Lt knee patient for five fractions. The orange colored horizontal line represents the intrafractional motion estimated from the pre- and post-treatment CBCT images. 89

Figure 25. An OBI image registered with digitally reconstructed radiography (DRR) image from a planning CT image. When the ROI was set to arm structure, shoulder structures misaligned from the reference position. 91

Figure 26. A comparison of correction result with respect to the derived setup errors by CBCT vs. ROIM for Lt. inner thigh patient. 93

Figure 27. A comparison of correction result with respect to the derived setup errors by CBCT vs. ROIM for Lt. knee patient. 94

CONTENTS

Abstract i

List of Tables iii

List of Figures v

General Introduction 1

Chapter I. Automated Mechanical Quality Assurance (AutoMQA) System for Medical Accelerators using Smartphone

Abstract 9

1. Introduction 11

2. Material and Methods

2.A. System description 13

2.B. Motion sensor signal processing module 18

2.B.a. Gyroscope 18

2.B.b. Accelerometer 18

2.B.c. Compass 19

2.B.d. Sensor fusion 19

2.C. Image processing module 23

2.C.a. Preprocessing of acquired image 23

2.C.b. Length calibration 25

2.C.c. Feature points detection 27

2.D. System evaluation experiment 28
2.D.a. System accuracy and precision – angle measurement with motion sensors 28
2.D.b. System accuracy and precision – length measurement by image processing 29
2.E. Clinical application: Monthly mechanical QA 31
2.E.a. Gantry rotation angle indicator 31
2.E.b. Collimator rotation angle indicator 31
2.E.c. Jaw position indicator 32
2.E.d. Crosshair centering 33
2.E.e. Optical distance indicator 33
3. Results
3.A. System accuracy and precision 38
3.B. Clinical application 41
4. Discussion 48
5. Conclusions 51

Chapter II. Real-time Optical Image-based Monitoring (ROIM) System for Radiotherapy

Abstract 53
1. Introduction 55
2. Material and Methods
2.A. System description 59
2.B. Infra-red stereo camera system 61
2.B.a. Hardware 61

2.B.b. Stereo camera calibration....63
2.B.c. 3D reconstruction....64
2.B.d. IR marker detection....65
2.B.e. Registration with planning CT images....67
2.C. System evaluation....69
2.D. Clinical application: Extremity STS patients....72
2.D.a. Measurement of inter-fractional motion....72
2.D.b. Measurement of intra-fractional motion....73
2.D.c. Multiple region of interest analysis....74
2.D.d. Comparison....74
3. Results
3.A. System evaluation....79
3.B. Clinical application....81
4. Discussion....95
5. Conclusions....99

General Discussion....100

Conclusions....102

References....103

GENERAL INTRODUCTION

The aim of the radiotherapy is to simultaneously maximize tumor dose and minimize normal tissue dose, thereby improving tumor control probability and reducing possible complications (Figure 1). To achieve this, various techniques have been developed and applied in clinical practice.

Recent advances in technologies for dynamic beam delivery and dose conformation have allowed increased clinical applications of high precision radiotherapy. In conventional radiotherapy techniques, a generous margin is commonly applied to compensate for inter-fractional errors, such as daily setup variations [1]. However, with high precision techniques such as intensity modulated radiotherapy (IMRT) and volumetric modulated arc therapy (VMAT), consistent geometrical setup of both the linear accelerator (LINAC) and patient has become a significant challenge [2,3].

Geometrical uncertainties can make the treatment beam miss the target volume and accidentally hit the healthy organs. Hence, consequently, the target volume receive less dose than therapeutic dose. This results in lower tumor control and higher complication probability.

The International Commission on Radiation Units and Measurements (ICRU) specifies three sources of geometrical uncertainty which may hinder precise delivery of a planned beam: (1) machine related errors, (2) patient set-up variations, and (3) organ motion.

Machine related errors are due to deviations of LINAC mechanical properties

from the desired values. High precision radiotherapy can be successful only if geometrical consistency of the LINAC mechanical properties, such as gantry rotation angle and jaw positions, are controlled to a high degree (Figure 2). Thus a reliable LINAC quality assurance (QA) program is essential.

Patient set-up variation is due to errors in the daily positioning of the patient for each treatment fraction. This is also called inter-fractional error.

Organ motion is the target volume displacement with respect to the desired iso-center during a single treatment fraction. This is also called intra-fractional error (Figure 3).

These deviations from the desired irradiation geometry may be systematic or random. Systematic errors occur if the mean treatment geometry in the fractionated treatment deviates from the planned geometry. Random errors are variation around the mean deviation. Based on these deviations, internal and set-up margins are applied to the target volume, following the van Herk formula [4,5].

Various efforts to assess these geometrical uncertainties have been reported, e.g. immobilizing and localizing patients on the treatment table. The most useful method is image guided radiotherapy (IGRT). For example, radio opaque markers are implanted in the tumor to track tumor movement with X-ray based imaging modalities such as cone beam computed tomography (CBCT). Other imaging modalities, such as ultrasound (US) or magnetic resonance imaging (MRI), have been studied. However, there remains some controversy about optimal modality and procedures to assess various geometric uncertainties.

In this dissertation, two systems to assess geometric uncertainties in

radiotherapy are described (Figure 4). Chapter I describes the proposed smartphone application for mechanical QA of LINAC to assess machine related errors. Chapter II describes the proposed optical image based guidance system using a stereo camera to assess patient motion related errors. These systems were adopted to a clinic to test clinical feasibility.

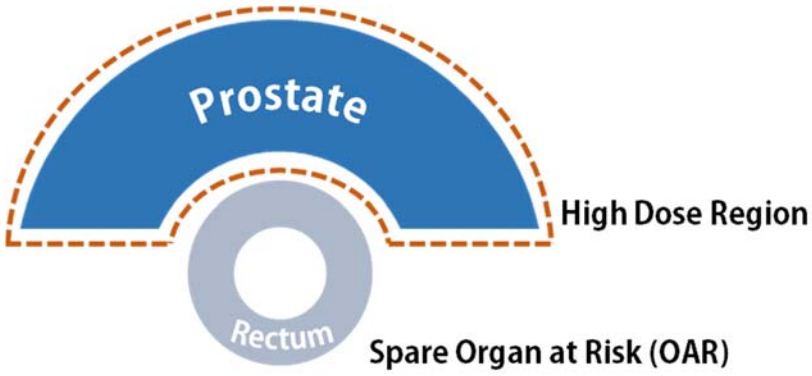

Figure 1. The aim of the radiotherapy is to maximize the tumor dose and to minimize normal tissue dose simultaneously thus improve tumor control probability and reduce complications. High dose region is fit to the target volume.

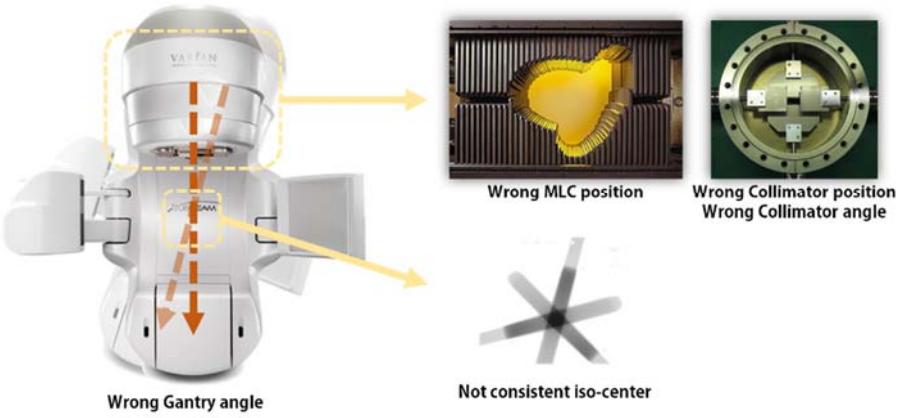

Figure 2. The geometric uncertainties related to machine errors. Machine related errors are due to deviations of mechanical properties of LINAC from the desired value. High-precision radiotherapy can be successful only if geometrical consistencies of the mechanical properties of LINAC such as gantry rotation angle and each jaw positions are insured to a high degree

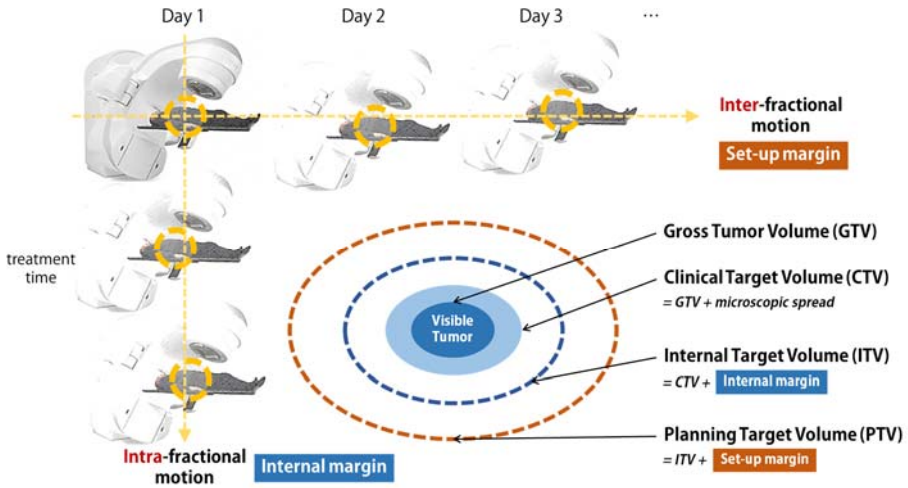

Figure 3. The geometric uncertainties related to the patient localization error. Patient set-up variation is due to errors in the daily positioning of the patient at each treatment fraction and it is called as inter-fractional error. Organ motion is the target volume displacement with respect to the treatment iso-center during a single fraction and this type of error is called as intra-fractional error. To assess those errors, internal margin and set-up margin is applied to the internal target volume and planning target volume, respectively.

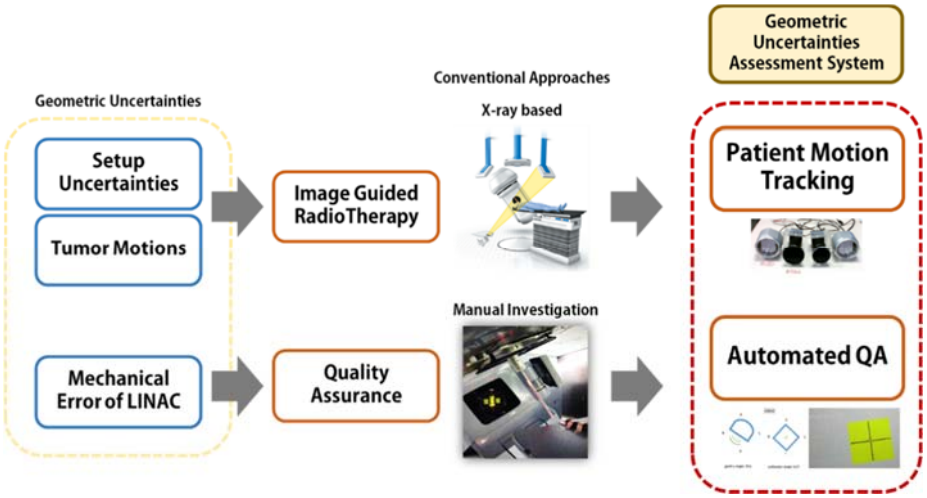

Figure 4. An overview of the developed geometric uncertainty assessment system for radiotherapy. First, in order to assess machine related errors, a smartphone application for mechanical QA of LINAC is developed. Second, in order to assess patient related motion errors, optical image-based guidance system using a stereo camera is developed. These systems were adopted to the clinic to test clinical feasibility.

Chapter I. Automated Mechanical Quality Assurance (AutoMQA) System for Medical Accelerators using Smartphone

Abstract

PURPOSE: Mechanical quality assurance (QA) of medical accelerators consists of a time consuming series of procedures. Since most procedures are performed manually, e.g. checking gantry rotation angle with the naked eye using a level attached to the gantry, it is a human error prone process. To avoid these inconveniences, we propose an automated mechanical QA system (AutoMQA) using a smartphone.

METHODS: The system consists of two smartphones, one (device) attached to the gantry to obtain real time information on mechanical parameters of the medical accelerator and field light images, and the other (controller) to control the system and display relevant data. The gyroscope, accelerometer, and magnetic field sensor embedded in the device smartphone were used to measure gantry and collimator angles. Images from the high resolution camera of the device smartphone were processed to evaluate jaw positioning, crosshair centering, and source to surface distance (SSD) accuracy. The application was developed using the Android software development kit and OpenCV library. AutoMQA accuracy and precision was validated against an optical rotation stage and digital calipers, then applied for QA measurements of two medical accelerators.

RESULTS: System accuracy and precision to measure angles and lengths were $0.08 \pm 0.06°$ and 0.42 ± 0.27 mm, respectively. The mean absolute errors (MAE) in QA measurements of gantry and collimator rotation were $0.08 \pm 0.07°$ and $0.09 \pm 0.07°$, respectively. The MAE in QA measurements of light field

sizes was 0.43 ± 0.33 mm. The MAEs in QA measurements of crosshair centering and SSD were 0.51 ± 0.22 mm and 0.79 ± 0.25 mm, respectively. Two fold decrease in mechanical QA duration was experienced using the AutoMQA system.

CONCLUSIONS: Most mechanical QA items recommended by AAPM TG142 can be tested using the proposed AutoMQA system with acceptable accuracy and precision. Embedding the AutoMQA system in a medical accelerator allows independent online monitoring of mechanical accuracy and should eliminate error prone and time consuming manual QA procedures.

1. Introduction

Angular and positional misalignment in mechanical parameters of medical linear accelerators (LINACs) may produce significant dosimetric deviation from the planned values [6]. During the treatment course, all the mechanical parameters should be consistent as planned within given tolerances. Operators depend on LINAC digital indicators to confirm this consistency, assuming that all indicators were fully validated prior to the treatment. Therefore, the American Association of Physicists in Medicine (AAPM) TG-142 recommended a list of quality assurance (QA) procedures and tolerances to maintain LINAC consistency [7].

Mechanical LINAC QA consists of a series of human error prone and time consuming procedures, because most procedures are performed manually, e.g. checking gantry rotation angle with the naked eye using a level attached to the gantry. Various automated mechanical QA programs and methods for medical LINAC have been reported to remove or reduce the opportunity for human errors and reduce procedure duration [8–20].

Most attempts to automate the QA procedures utilize X-ray based systems, such as electronic portal imaging device (EPID) or radiochromic films [9,10,12,14,16–18]. Winkler *et al.* described the auto-control system of EPID based rotation axes, collimator and laser adjustment [10]. Rowshanfarzad *et al.* also introduced various EPID based machine verification systems to assess

gantry angle and multi-leaf collimator (MLC) positions [16–18]. While these X-ray based systems can precisely assess rotation axes and jaw positions independently, the procedures remain highly sensitive to the detector's spatial resolution and a high degree of human effort is required for the measurements.

Others proposed custom devices rather than X-ray based systems. Arjomandy *et al.* developed a cube shaped in-house device to measure rotation axis location and wobble precisely; Welsh *et al.* assembled digital inclinometers and digital tape for measuring gantry and collimator angles and optical distance indicator (ODI) verification [21]. These types of customized equipment worked well in practice, but were only available in a few clinics.

A smartphone is a representative example of condensed technology. They offer a variety of methods to access information around the user through a high resolution camera and various sensitive sensors. The sensors are a unique feature that distinguishes smartphones from other computer devices. Consequently, smartphones have been widely used for health care applications [22,23], such as clinical decision support systems [24–26], patient monitoring systems [27,28], surgery assistance, etc. [29].

We propose an automated mechanical QA system (AutoMQA) for medical LINACs using a smartphone. To the best of our knowledge, this is the first smartphone application for comprehensive mechanical QA of the items recommended by AAPM TG-142. The system overview is described in Chapter 2.A, and Chapters 2.B and 2.C describe two implemented modules, motion

sensor signal processing and image processing. The system was tested against an optical rotation stage and digital calipers to determine the accuracy and precision (Chapters 2.D and 3.A), prior to QA measurements of the LINAC mechanical parameters listed in AAPM TG-142 (Chapters 2.E and 3.B). The discussion and conclusions follow.

2. Material and Methods

2.A. System description

As recommended in the AAPM TG-142 report, mechanical QA of LINAC consists of various procedures to maintain geometric consistency regarding gantry and collimator rotation angles, jaw-positioning, crosshair-centering, and source-to-surface distance (SSD) using ODI [7]. With motion sensors and a high-resolution camera embedded in a smartphone, the AutoMQA system was developed.

The system consisted of two smartphones; one (device) attached to the gantry to obtain real-time information on mechanical parameters of medical accelerator and images of field light, and the other (controller) communicated with the device via wireless network (specifically, Bluetooth®) to control the system and to display obtained data. The AutoMQA system consists of two main modules: (1) motion sensor signal processing module, (2) optical image processing module. The application was developed with the Android software development kit (SDK) and OpenCV library. In this study, the Galaxy note 3 (Samsung electronics Co. Ltd., South Korea) smartphone was used. Figure 5 shows a schematic of the system.

(1) **Motion sensor signal processing module:** Three motion sensors (gyroscope, accelerator, and magnetic field sensor) embedded in the

smartphone were used to measure gantry and collimator angles. It was assumed that the roll rotation axis of the smartphone is perpendicular to the central axis (CAX) of the medical accelerator (Figure 6). Hence, the rotation angle of the smartphone refers to that of the gantry or the collimator. A combination use of several different sensors (known as sensor fusion method) enhanced the accuracy of determining the orientation of the smartphone with respect to the gravity [30] (the detail is described in sec. 2.B).

(2) **Optical image processing module:** An optical-image processing module using an image taken by the high-resolution camera was developed to assess jaw-positioning, crosshair-centering, and SSD. The camera was calibrated and a series of image processing steps applied for determining the locations of feature points such as crosshair-center and edges of X-and Y- jaws (the detail is described in sec. 2.C).

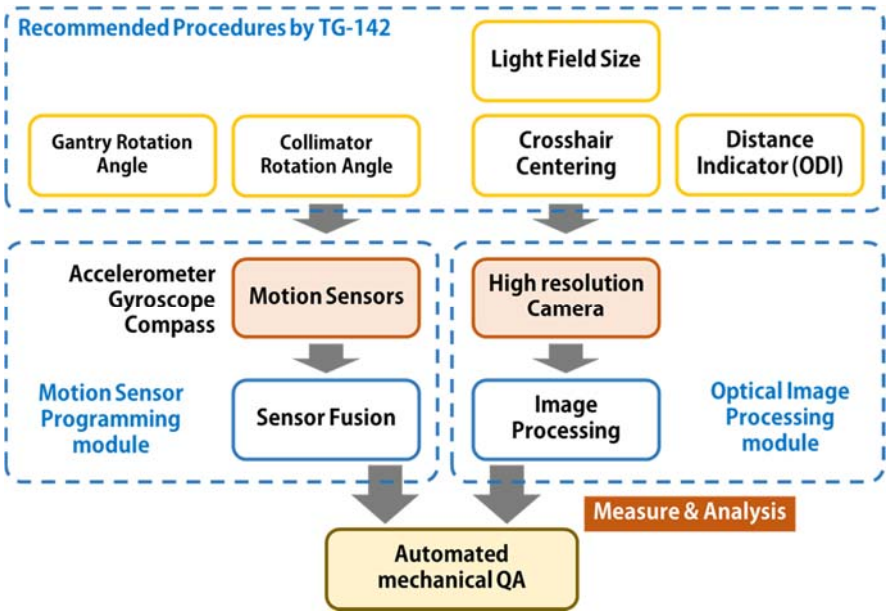

Figure 5. A schematic of the AutoMQA system. The system is consisted of two main modules. The one is the motion sensor signal processing module which is for the gantry and the collimator rotation angle measurements by using various motion sensors embedded in a smartphone. The other is the optical image processing module which is for the jaw position, crosshair position, and SSD measurements by using high-resolution camera embedded in a smartphone.

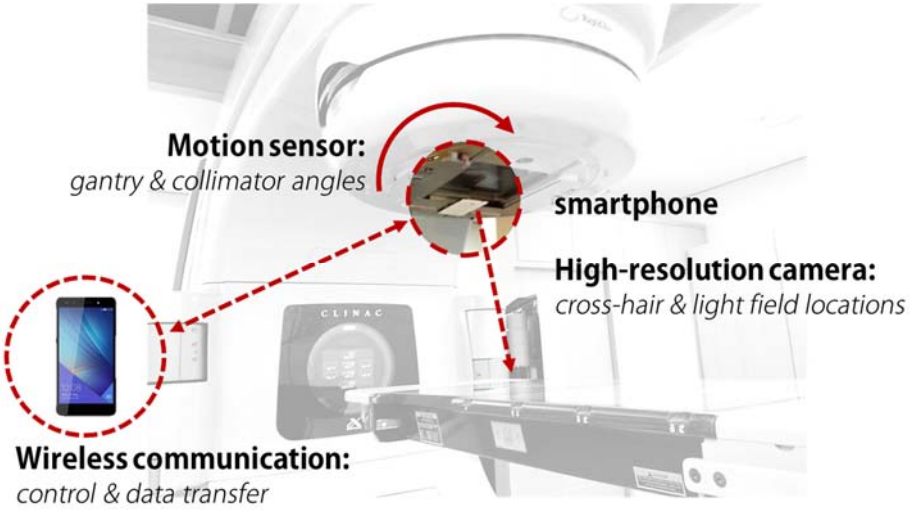

Figure 6. A smartphone attached to the LINAC gantry, and the roll rotation axis of the smartphone is perpendicular to the central axis (CAX) of the medical accelerator. In order to control and receive the measured data from the device attached to the gantry, wireless communication module was implemented to make connection between another smartphone and the device via wireless network, specifically, Bluetooth®.

2.B. Motion sensor signal processing module

2.B.a. Gyroscope

A gyroscope sensor is designed to measure the Coriolis force due to rotation, instead of measuring acceleration. The Coriolis force acts only while the smartphone rotates, therefore it measures only the angular velocity of the smartphone [31].

A gyroscope immediately responses when the smartphone is rotated, however, it has some drawbacks. First, when the smartphone is stationary, regardless of the smartphone's orientation, gyroscope signal always indicates zero. Thus, the absolute orientation with respect to the gravity cannot be measured by using a gyroscope. Second, to derive a rotation angle of the smartphone, gyroscope values are integrated over time; however, the values include noise and the offset are integrated as well. This results in a long-term drift in the calculated angle, which if not addressed would make the integrated value be far from the real value [31]. These drawbacks would be compensated by using the information from other sensors (sensor fusion method), and the detail is described in section 2.B.d.

2.B.b. Accelerometer

Every object on Earth feels the downward force of gravity, thus the mass is also pulled downward by the gravity and springs deform, allowing acceleration due to the gravity to be measured. At rest, an accelerometer measures only the force of gravity [31]. During rotation, the smartphone measures the force that caused it to accelerate, thus the absolute orientation of the smartphone with

respect to the gravity can be measured. However, accelerometer signal is quite noisy so it needs a low-pass filter for the signal processing.

2.B.c. Compass

Most of compass sensors are a kind of Lorentz force sensors, and thus measure a mechanical displacement of the wire rather than a voltage across it. Regardless of the physical mechanism, compass sensors will derive the magnetic field in each axis [31]. However, the magnetic field readout is quite noisy and may seem less accurate especially in the treatment room environment where many electronic devices emit RF signal and noise.

2.B.d. Sensor fusion

In general, a sensor fusion method is a process to combine more than one sensor to obtain better output [30, 32]. The gyroscope provides a low-noise rotation angle measurement; however, it does not correspond to the absolute orientation of the smartphone. Despite its ability of deriving the absolute orientation of the smartphone, the accelerometer may produce excessive noise. Smoothing such noise with a low-pass filter results in response delay. Therefore, a sensor fusion method primarily uses the integrated gyroscope signal (relative orientation), and prevents it from drifting by constantly correcting it with the accelerometer signals to gain an absolute orientation of the smartphone with respect to the gravity (Figure 7).

Those motion sensors which represents a 3D-rotation can easily be fused together if the correct representation is chosen. Different formats can be used to represent a rotation of a rigid body in the 3D-space:

- *Euler-Angles:* Three rotations-angles (yaw, pitch and roll) along predefined axis. Euler-Angles have the benefit of being easy to interpret, but suffer from certain limitations, such as gimbal lock or the lack of the possibility to interpolate between two rotations described in Euler-Angles.

- *Rotation Vector:* A more general form that can represent an arbitrary rotation by specifying a rotation-axis with three components x, y, z and a rotation angle α around this axis.

- *Rotation Matrix:* A 3x3 matrix that can be used directly for rendering rotations. It is very often used in computer graphics, because it can be combined with other transformations and efficiently applied by parallel multiplications.

- *Quaternions:* A closely related representation to the rotation vector; when given a rotation angle and rotation axis x, y, z, quaternions represent them as:

  $$q = \cos\frac{\alpha}{2} + i(x \cdot \sin\frac{\alpha}{2}) + j(y \cdot \sin\frac{\alpha}{2}) + k(z \cdot \sin\frac{\alpha}{2})$$

  On the first sight, this makes the representation more complex, but Quaternions other a mathematically elegant way of interpolating between two Quaternions, called Spherical Linear Interpolation (SLERP).

Quaternion SLERP, from here on denoted as $\oplus$ can furthermore be used to extrapolate or perform a weighted interpolation between two Quaternions, where a is the weight of each component into the interpolation (with a being a value between 0 and 1):

$$Quaternion_{interpolated} = a \cdot Quarternion_1 \oplus (1 - a) \cdot Quarternion_2$$

A low-pass filter smooths jittery signals by averaging over a number of measurements. The bigger this set, the smoother the signal but at the cost of higher latency. It is used for processing data from the accelerometer and the compass. A high-pass filter on the other hand works like a gate that only lets through a value if it has changed enough compared to its previous value. Since gyroscopes only measure velocities, they require an integration-stage to deliver an orientation. During this integration, noise is transformed into drift which can be eliminated with a high-pass filter.

The calibrated gyroscope measures changes in rotation, so these changes need to be integrated to obtain an orientation (represented as Quaternion); the orientation sensor already outputs Quaternions. So the simplest way of fusing both is to perform a Quaternion SLERP:

$$Orientation\ Sensor = Gyroscope \cdot w \oplus RotationVector \cdot (1 - w)$$

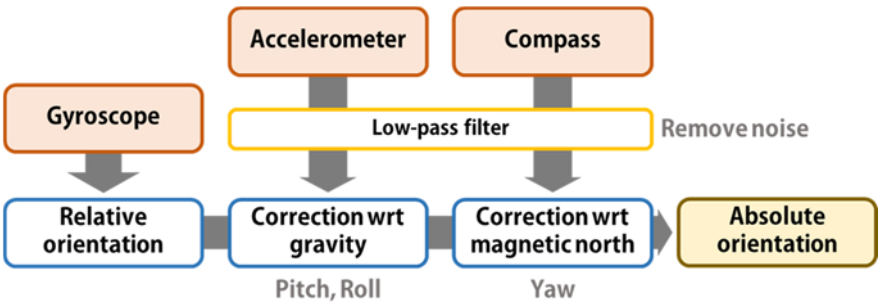

Figure 7. A process of sensor fusion method. The relative orientation of a smartphone is determined by a gyroscope primarily which measures angular velocity. Thereafter, relative orientation is corrected by an accelerometer or a compass to derive absolute orientation of a smartphone. The noises of signals from the accelerometer and the compass were removed by low-pass filters.

2.C. Image processing module

2.C.a. Preprocessing of acquired image

In order to acquire exact size or location of jaw openings from light field image projected on the treatment couch, image preprocessing is needed. Image pre-processing can significantly increase the reliability of an optical inspection. Various filter operations which intensify or reduce certain image details enable an easier and precise evaluation.

Light field and a crosshair were recognized by the Canny edge detection method using a gray-scale image taken by the high-resolution camera (Figure 8).

First, we acquired gray-scale image from 16 bit RGB image by normalization to eliminate illumination effect, thereafter, a binary image was created by thresholding with the half of maximum intensity as a threshold – thus, the image was segmented to obtain full width half maximum (FWHM) of light field.

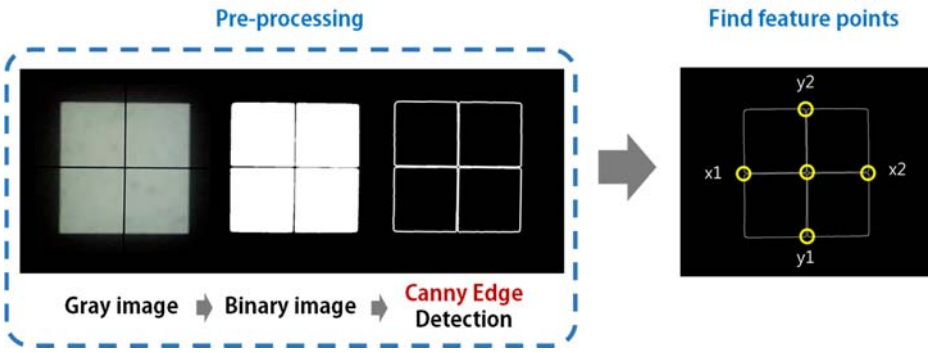

Figure 8. The process of the image preprocessing module. Light field and a cross-hair were recognized by the Canny method using a gray-scale image taken by the high-resolution camera. Then feature points were detected by the Harris method to calculate the locations of each of the jaws and the cross-hair.

2.C.b. Length calibration

In order to measure the absolute length from an image, images of a known geometry (herein a 100 KRW coin) were taken. A circle detection module was implemented using the Hough transform method to determine the radius of the circle [33].

Hough transform for a range of radii is computed and the radius corresponding to the maximum intensity at each pixel is determined. If this maximum intensity exceeds some threshold, the pixel is assigned the value of the associated radius and if the maximum intensity is below the threshold, the pixel is assigned a value of 0. A closing operation is then performed to produce a closed region of radius values centered at the center of the coin.

With the determined radius, we can get a calibration factor as below.

$$\text{Calibration factor} = {real\ length\ (mm)}\Big/{length\ from\ the\ acquired\ image\ (px)}$$

If the radius of the known geometry is 12 mm and determined radius from the acquired image is 50 px, the calibration factor becomes 0.24 mm/px.

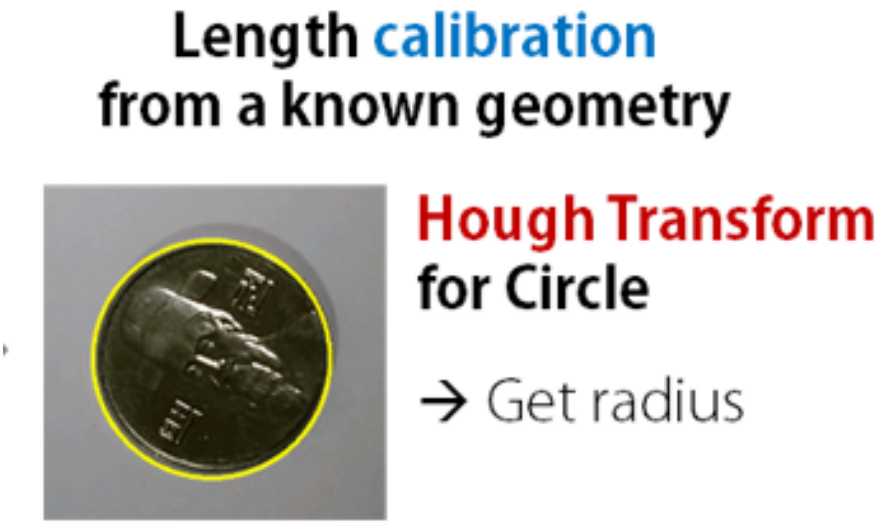

Figure 9. A screen shot example of length calibration. The calibration factor was caclualted with the radius determined by detecting a circle (known geometry, for this example, 100 KRW) by using Hough transform algorithm.

2.C.c. Feature points detection

The Harris corner detection method was employed to produce second partial derivatives of image intensities. It derives Hessian matrix with second partial derivatives [34].

$$\mathrm{A} = \sum_{u}\sum_{v} w(u,v)\begin{bmatrix} I_x^2 & I_xI_y \\ I_xI_y & I_y^2 \end{bmatrix} = \begin{bmatrix} \langle I_x^2 \rangle & \langle I_xI_y \rangle \\ \langle I_xI_y \rangle & \langle I_y^2 \rangle \end{bmatrix}$$

For corners, the matrix is characterized by two large eigenvalues, thus we can get best features from the edge image (Figure 8). Top five best features were the crosshair and four each jaw's end.

In order to refine the corner locations in sub-pixel accuracy, the intensity gradient from the gray-scale image was calculated near each corner. Given the fact that dot product between two vectors perpendicular to each other is zero, several equations were made and solved using the candidate points near the detected corner by the Harris method.

2.D. System evaluation experiment

The object of this evaluation was to determine the accuracy and precision of the system prior to tests on LINAC. In order to exclude errors due to the gantry sag or other sources, a smartphone itself was used for evaluation – not attached on the gantry. We derived the mean absolute error (MAE) and the standard deviation (SD) of the test sets to determine the accuracy and precision of the system.

Mean error: $\mathrm{MAE} = \bar{e} = \frac{\sum |\Delta e_i|}{n}$, where Δe_i is error of i-th test and n is the number of tests.

Standard deviation: $\mathrm{SD} = \sqrt{\frac{\sum (\Delta e_i - \bar{e})^2}{n}}$, where $\bar{e}$ is mean absolute error.

By comparing the derived system accuracy and precision with the tolerances recommended by the AAPM TG-142 report, the feasibility of clinical application of the AutoMQA system was validated.

2.D.a. System accuracy and precision – angle measurement with motion sensors

The accuracy and precision of the system for angle measurements were evaluated by measuring various orientations of the smartphone attached to the optical rotation stage (ST1-418-B4, Sciencetown, South Korea). The roll rotation angle of the smartphone refers to the gantry rotation angle and the yaw rotation angle of the smartphone facing rightward refers to the collimator

rotation angle (Figure 10 left). The tests were performed at various angles set up with the optical rotation stage. For the roll rotation, the optical rotation stage offers -20° to 20° rotations with an 1° resolution and a 0.03° precision. For the yaw rotation, we measured 0° to 270° rotations of the smartphone attached to the optical rotation stage with a 0.1° resolution and a 0.003° precision. Test sets included ten known rotations and each of them was repeated three times to confirm the reproducibility of the system. We derived MAE and SD of total ten test sets.

2.D.b. System accuracy and precision – length measurement by image processing

The accuracy and precision for length measurements were evaluated by measuring the sizes of ten test templates (5×5 cm^2, 7×7 cm^2, 9.5×9.5 cm^2, 9.8×9.8 cm^2, 10×10 cm^2, 10.2×10.2 cm^2, 10.5×10.5 cm^2, 12×12 cm^2, 15×15 cm^2, and 20×20 cm^2 squares) at the camera to template distance of 50 cm, following the calibration with a known geometry of 5 cm radius circle. Each template size was confirmed by using the digital calipers with a 0.03 mm precision (Absolute 500, Mitutoyo, IL, USA) (Figure 10 right). Each of the test sets was repeated three times to confirm the reproducibility of the system. We derived MAE and SD of total ten test sets.

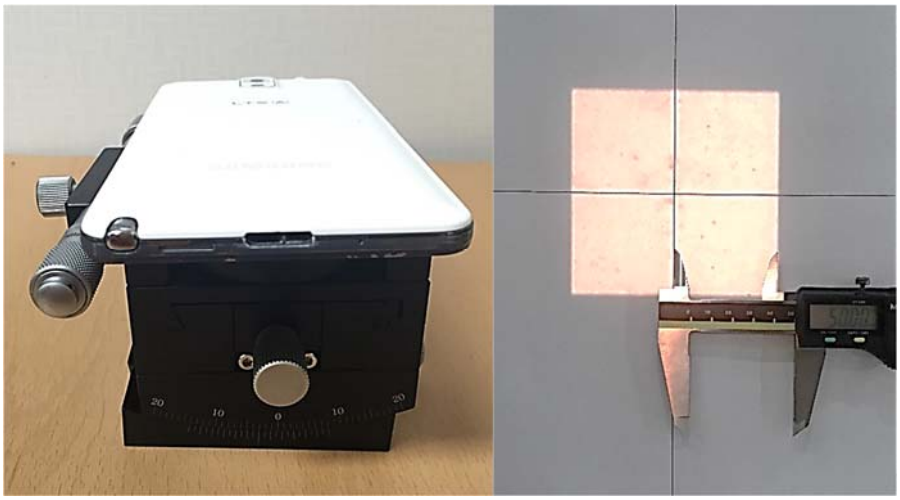

Figure 10. An evaluation of the AutoMQA system accuracy. Motion sensor signal accuracy was evaluated by measuring orientation of the smartphone attached to the optical rotation stage and compared with the actual angle indicated by the optical stage (left). Image processing accuracy was evaluated by measuring template sizes of ten test sets at the source to surface distance of 100 cm following the calibration procedure with a 5 cm radius circle template (right).

2.E. Clinical application: Monthly mechanical QA

We performed monthly mechanical QA procedures recommended by AAPM TG 142 using the AutoMQA system to confirm its feasibility of clinical application on LINAC. The tests were performed with two Varian 6EX and 21IX medical LINACs (Varian Medical Systems, CA, USA) installed at Seoul National University Hospital (SNUH) and Jeju National University Hospital (JNUH), respectively.

2.E.a. Gantry rotation angle indicator

It was assumed that the roll rotation axis of the smartphone is perpendicular to the central axis (CAX) of the medical accelerator. Hence, the rotation angle of the smartphone refers to that of the gantry.

Gantry rotation angles were measured at the gantry angles of 0, 90, 180, and 270 degrees. The measured angles were compared to values on the digital indicator of LINAC and confirmed the consistency with a bubble level (manual method).

Each of test sets was repeated three times to confirm the reproducibility of the system. We derived the MAE and SD of total ten test sets.

2.E.b. Collimator rotation angle indicator

We can measure a collimator rotation angle by measuring yaw rotation angle

of a smartphone at gantry angle of 0°. However, it is not recommended because of high noise due to the LINAC. This large electronic device interrupts the geomagnetic signal, thus signal from the compass sensor will be inaccurate. Therefore, we used yaw rotation angle of a smartphone at gantry angle of 90° – the smartphone facing rightward. At this position, we can get the absolute yaw rotation angle of the smartphone with respect to gravity and this refers to the angle of the collimator.

Collimator rotation angles were measured at the collimator angles of 0, 90, and 270 degrees (180° is not allowed to the collimator rotation). The measured angles were compared to digital indicator of LINAC and confirmed the consistency with a bubble level.

Each of test sets was repeated three times to confirm the reproducibility of the system. We derived MAE of total ten iterations of test set.

2.E.c. Jaw position indicator assessment

From the determined location of the feature points as described in section II.C.3, we can measure light field size by calculating distance between crosshair and each jaw positions. Measured length can be calculated using the calibration factor as follows:

$$Measured\ length\ (mm) = Image\ length\ (px) \times Calibration\ factor\ (mm/px)$$

Each jaw position was measured at SSD of 100 cm, and field size of 10×10 cm^2. Thereafter, we intentionally changed the field size asymmetrically to check the feasibility of detecting field size discrepancies. Each jaw positions were confirmed by using digital calipers (0.01 mm precision). Each of test sets was repeated three times to confirm the reproducibility of the system. We derived MAE of total ten test sets.

2.E.d. Crosshair centering

The object of this experiment was to determine the precision for the crosshair centering consistency measurement of the AutoMQA system. The system can track the real-time position of crosshair with video mode, thus maximum deviation from the initial position of the crosshair (crosshair location at collimator angle of 0°) was measured (Figure 11).

Each of test sets was repeated three times to confirm the reproducibility of the system. We derived MAE of total ten iteration of test sets.

.

2.E.e. Optical distance indicator

It was assumed that the smartphone was parallel to the image of field size projected on the treatment couch and lens distortion was negligible. The pinhole

camera model defines the mathematical relationship between real geometry and that of projected on the image plane (Figure 12).

In order to calculate a camera-to-surface distance (CSD), simple formula can be derived as follows and all the device-related specification was from the manufacturer of the smartphone:

$$\mathrm{CSD} = \mathrm{F}\frac{RL \times FL}{IL \times SL}$$

F: focal length (mm) = 4.13 by specification

FL: frame length (px) = 1920 by camera setting

SL: sensor length (mm) = 4.69 by specification

RL: real length (mm) = 100 where SSD = 100 cm, FS = 10×10 cm^2

IL: measured length by image processing (px)

Finally, SSD can be derived from calculated CSD by simply adding source-to-camera distance (SCD). In this study, SCD is initially assumed as 60 cm for the LINAC we tested as specified in Monte Carlo simulation package provided by the manufacturer. To confirm and calibrate some parameters such as SCD and focal length, nine combinations of parameters were tested. We precisely fixed SSD at 100 cm and field size as 10×10 cm^2 by using a well-calibrated front-pointer and digital calipers. Discrepancies between measured field size and actual field size (10×10 cm^2) were measured with various combinations of SCD and focal length.

The SSD measured with this system was compared to the SSD measured with well-calibrated front-pointers for 100 cm and 110 cm. Total ten test sets were performed for various values of SSD.

To assess the accuracy of the SSD measurement, we verified the measured SSD with this system by comparing the SSD measured with well-calibrated front-pointers for the SSD of 100 cm and 110 cm. Total ten test sets were performed for each assessment.

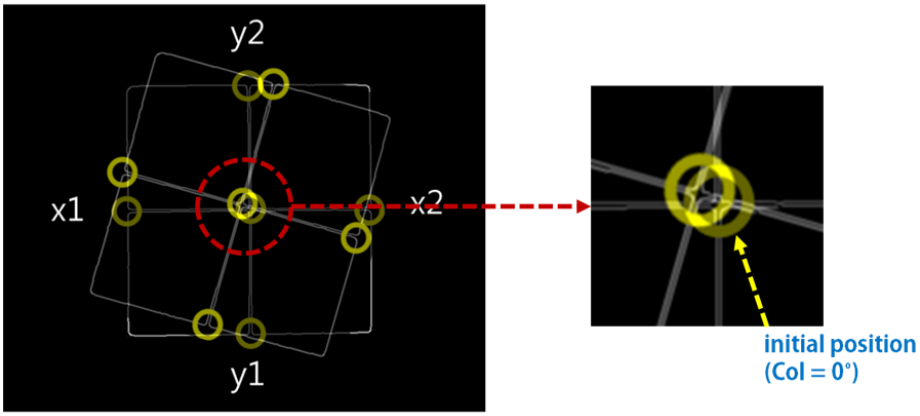

Figure 11. The AutoMQA system can track the real-time position of crosshair with video mode, thus maximum deviation from the initial position of the crosshair (crosshair location at collimator angle of 0°) can be measured.

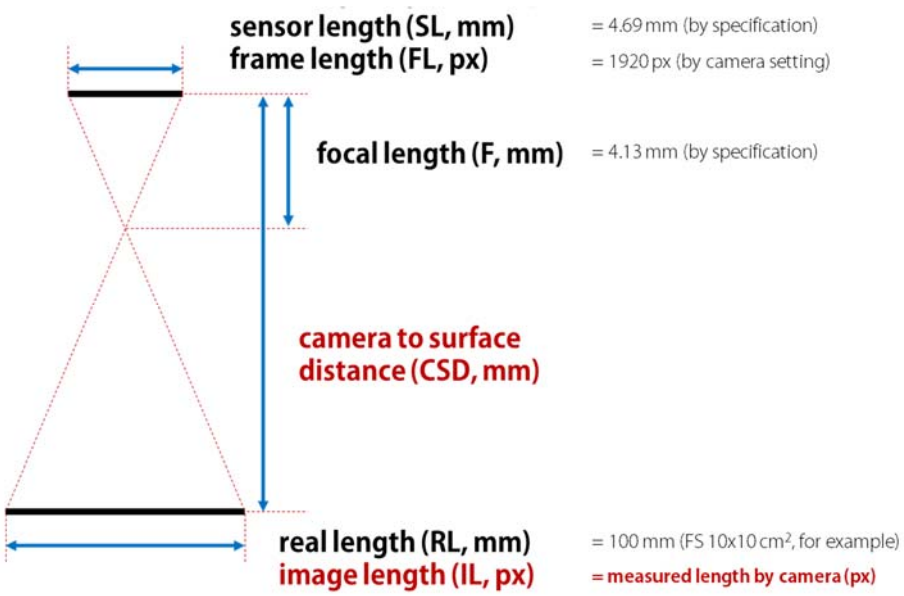

Figure 12. The mathematical relationship between real geometry and one projected on the image plane to derive camera-to-surface distance (CSD).

3. Results

3.A. System accuracy and precision

The accuracy and precision of the AutoMQA system to measure angles and lengths in terms of MAE were 0.08° ± 0.06° and 0.42 mm ± 0.27 mm, respectively. According to the AAPM TG-142 report, the tolerance values for gantry/collimator angles were 1.0° and those for the length measurements including jaw positioning (asymmetric), cross-hair centering, and optical distance indicator were 1.0 mm. Thus, the accuracy and precision of the AutoMQA system would be sufficient to test the mechanical QA items recommended by AAPM TG-142. The detailed results of the system accuracy and precision for angle and length measurements are described in 3.A.a and 3.A.b.

3.A.a. System accuracy and precision – angle measurement with motion sensors

The results of the system accuracy and precision for the rotation angle measurements for gantry (roll) and collimator (yaw) are shown in TABLE 1. The MAEs with a standard deviation (SD) of rotation angle measurements were 0.09° ± 0.06° and 0.08° ± 0.06° for roll and yaw rotations, respectively. The maximum absolute error was 0.23° and 0.22°, respectively. Even though the motion sensor resolution specified by the manufacturer (MPU6500, Invensense Inc., CA, USA) was 0.0036°, the system precision was intentionally adjusted

to the level of 0.1° due to high-sensitivity to noise at high-precision.

3.A.b. System accuracy and precision – length measurement by image processing

The result of the system accuracy and precision for the field size measurement with various test templates is shown in TABLE 1. With the camera resolution of 4128×3096, the calibration factor was 0.107 mm/px when the system was calibrated by using the known geometry of 5 cm radius circle. The MAEs with SD of field size for each X and Y direction were 0.39 mm ± 0.26 mm and 0.44 mm ± 0.28 mm, respectively. The total MAE with SD for various reference field sizes was 0.42 mm ± 0.27 mm. The maximum absolute error was 0.98 mm.

TABLE 1. System accuracy and precision: mean absolute errors and standard deviations of measured rotation angles (top) and lengths (bottom) for ten test sets. The other sources of error such as gantry sag were excluded.

N=10	Gantry angle (°)	Collimator angle (°)
MAE ± SD	0.09 ± 0.06	0.08 ± 0.06
Max (abs.)	0.23	0.22

N=10 / ME	Field size (mm)		
	X	Y	Total
MAE ± SD	0.39 ± 0.26	0.44 ± 0.28	0.42 ± 0.27
Max (abs.)	0.95	0.98	0.98

Abbreviations: MAE = mean absolute error; SD = standard deviation; Max = maximum error

Notes: Maximum errors were calculated in absolute terms

3.B. Clinical application: Monthly mechanical QA

TABLE 2 shows the comparison between the AutoMQA and manual results for the assessment of some mechanical QA items recommended by AAPM TG-142. For all items listed, the automated assessment with AutoMQA shows superior results to the manual assessment in terms of precision. There was no significant difference between the results of two LINACs. With the AutoMQA system, the total time taken for the mechanical QA procedures was reduced into approximately a half of the time taken manually. The detailed results of the assessment for each item are described in 3.B.a to 3.B.d.

3.B.a. Gantry and collimator rotation angle indicator

All the angles measured with the AutoMQA system were consistent with those of indicated by the bubble level (Figure 13). The accuracy and precision of the system was below 0.1°. The system can be regarded as a replacement for the manual method. The AutoMQA system always showed better accuracy and precision than the manual method. The system can also display the absolute angles of the gantry and collimator rotation with respect to the gravity within 0.1° precision.

3.B.b. Jaw position indicator

The result for jaw position indicator assessment with standard setup (SSD = 100 cm, FS = 10×10cm^2) is shown in TABLE 3. The MAEs for each jaws were ranged from 0.19 mm to 0.38 mm. Total MAE was 0.27 ± 0.14 SD. The RMSE was 0.35 mm.

The result for jaw position indicator assessment with intentional changes in each X and Y jaw positions are as follows: The MAEs with SD of field size for each X and Y direction were 0.31 mm ± 0.26 mm and 0.55 mm ± 0.35 mm, respectively. Total MAE was 0.43 mm ± 0.33 mm. The measured results of independent X and Y jaw positions for the positional errors are shown in TABLE 4. As described in 2.C.a, a binary threshold was the half of maximum intensity at the edge of light field, thus we could eliminate the source of human error in identifying the FWHM.

3.B.c. Crosshair centering

The system well tracked the crosshair in real-time and the MAE of maximum measured deviations was below 1 mm (≤ 5 px). The manual method involves drawing several crosslines to measure the offset of crosshair location and human error is possible during this procedure.

3.B.d. Optical distance indicator

The focal length and SCD were optimized by testing with nine combinations of parameters listed in TABLE 5. The system accuracy was best when the SCD and focal length were set to 600.1 mm and 4.12 mm, respectively. With these parameters, we performed the actual ODI assessment.

The MAE with SD of the measured SSDs was 0.79 mm ± 0.25 mm over ten test sets. The system was also consistent with the measurement using front pointers, thus the system can be regarded as a replacement for the manual method.

TABLE 2. Comparison between the AutoMQA and manual results for the assessment of some mechanical QA items recommended by AAPM TG-142. We derived MAEs of measurements and measured total time taken by each method.

Mechanical QA items (recommended by TG-142)	MAE			
	6EX		21IX	
	Manual	AutoMQA	Manual	AutoMQA
Gantry rotation angle indicator (°)	0.15 ± 0.10	0.09 ± 0.08	0.17 ± 0.11	0.08 ± 0.06
Collimator rotation angle indicator (°)	0.13 ± 0.12	0.09 ± 0.06	0.13 ± 0.11	0.09 ± 0.09
Jaw position indicator (mm)	0.85 ± 0.41	0.46 ± 0.27	0.80 ± 0.52	0.40 ± 0.39
Crosshair centering (mm)	0.75 ± 0.42	0.54 ± 0.21	0.85 ± 0.47	0.49 ± 0.23
Optical distance indicator (mm)	1.05 ± 0.55	0.84 ± 0.26	1.15 ± 0.47	0.74 ± 0.26
Duration	33 min 58 s	15 min 30 s	32 min 10 s	14 min 19 s

Abbreviations: MAE = mean absolute error

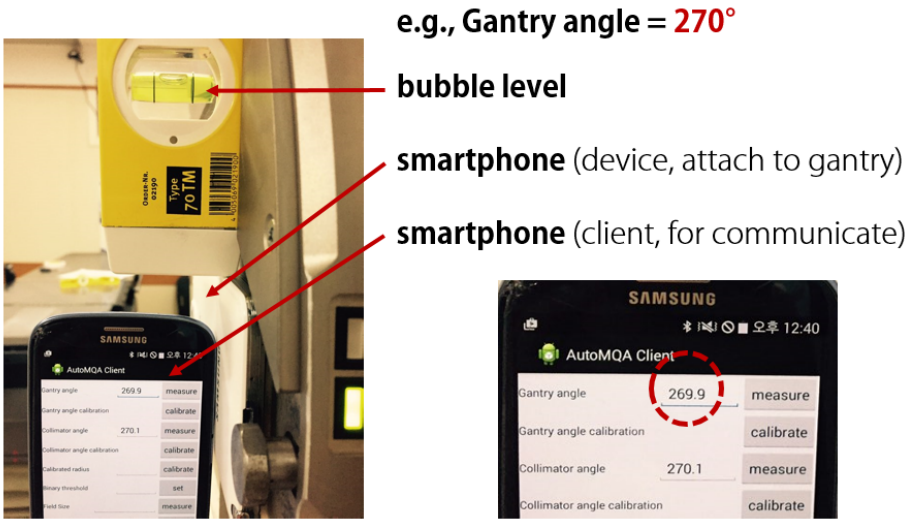

Figure 13. A gantry rotation angle was assessed with the AutoMQA system and showed proven accuracy. AutoMQA system showed consistent result with the bubble level.

TABLE 3. Jaw position measurement result for standard setup (SSD = 100 cm, FS = 10×10cm^2). Measured lengths were derived from the image length on the acquired image multiplied by calibration factor and averaged over total ten test results.

N = 10	Average image length (px)	Average measured length (mm)	MAE ± SD (mm)
X1	215.5	49.7	0.30 ± 0.16
X2	216.0	49.9	0.19 ± 0.09
Y1	215.0	49.6	0.38 ± 0.14
Y2	216.0	49.9	0.22 ± 0.10
Total	-	-	0.27 ± 0.14

Abbreviations: MAE = mean absolute error; SD = standard deviation;

TABLE 4. Independent jaw position measurement result for the tests applied various intentional error. The intended errors were noted as (X jaw displacement, Y jaw displacement).

Intentional errors (cm)	Absolute error (mm)				MAE ± SD (mm)
	X1	X2	Y1	Y2	
(1, 0)	0.2	0.1	0.8	0.2	0.33 ± 0.32
(-1, 0)	0.0	0.3	1.0	0.3	0.40 ± 0.42
(0, 1)	1.0	0.3	0.6	1.0	0.7 ± 0.34
(0, -1)	0.2	0.4	1.0	0.3	0.48 ± 0.36
(1, 1)	0.2	0.3	0.4	0.0	0.23 ± 0.17
(1, -1)	0.5	0.2	1.0	0.6	0.58 ± 0.33
(-1, 1)	0.6	0.5	1.0	0.3	0.60 ± 0.29
(-1, -1)	0.2	0.0	0.9	0.7	0.45 ± 0.42
(0.5, 0.5)	0.8	0.1	0.0	0.4	0.3 ± 0.36
(-0.5, -0.5)	0.1	0.1	0.3	0.2	0.18 ± 0.10
MAE ± SD (mm)	0.38 ± 0.33	0.23 ± 0.16	0.7 ± 0.36	0.4 ± 0.29	0.43 ± 0.33

Abbreviations: MAE = mean absolute error; SD = standard deviation;

TABLE 5. Optimal parameter verification test: The differences for each case were discrepancies between measured field size and desired field size.

SCD (mm)	Focal length (mm)	Diff. (mm)
599.9	4.12	0.42
599.9	4.13	-0.55
599.9	4.14	-1.52
600.0	4.12	0.32
600.0	4.13	-0.65
600.0	4.14	-1.62
600.1	4.12	0.22
600.1	4.13	-0.75
600.1	4.14	-1.72

Abbreviations: SCD = source to camera distance; Diff = difference

4. Discussion

Several smartphone applications for radiotherapy have been introduced recently. Ono *et al.* utilized the smartphone motion sensor for patient respiratory monitoring [35], and Schiefer *et al.* measured iso-center path characteristics of the gantry rotation axis using a smartphone camera, greatly reducing the burden of the Winston-Lutz test [36]. However, these applications required additional axillary devices and were not a comprehensive approach for radiotherapy QA.

Welsh *et al.* proposed a single platform assembled variety of QA tools, such as digital inclinometers [21]. The proposed device was shown to be stable and accurate in clinical tests. However, system and axillary device was still prone to human errors for some QA procedures, such as field size assessment and ODI verification.

To the best of our knowledge, the AutoMQA system proposed here is the first smartphone application to comprehensively address the routine mechanical QA process recommended in AAPM TG 142. It does not require specialized equipment or axillary devices, allowing anyone to adopt this method to the clinic by simply installing the application on a suitable smartphone.

Combination of three motion sensors (sensor fusion) enhanced the accuracy and precision of determining the smartphone orientation with respect to gravity, and allowed measurement of any gantry/collimator orientation angle. [30] Image processing guaranteed the accuracy and precision of measuring the

length of the features, e.g. crosshair location or jaw positions, on the acquired image. TABLE 6 shows the list of mechanical QA items recommended by TG-142, and identifies the availability with AutoMQA system. AutoMQA system accuracy and precision were determined using an optical rotation stage as acceptable to perform periodic QA procedures to check the accuracy of digital (or optical) indicators of medical accelerators.

With the proposed system, manual QA procedures using a level and a ruler can be automated, potential human errors eliminated, and the time required for mechanical QA reduced two fold. System accuracy and precision could be improved using later model smartphones with more advanced motion sensors and higher resolution cameras. Careful initial calibration is strongly recommended, because this AutoMQA system assumes the rotational axes of the smartphone attached to the gantry are perfectly perpendicular to the beam path. To achieve more reliable and reproducible setup, well fabricated smartphone holders for various LINAC models are required.

Currently, there is no available system for independent online monitoring of the digital (optical) indicators of LINAC mechanical parameters. During treatment, operators must rely only on the values displayed by various LINAC indicators. However, if the AutoMQA system is embedded into a medical accelerator, independent online monitoring of mechanical accuracy can be provided, eventually eliminating time consuming periodic QA procedures. Modules to synchronize with the digital indicators of LINAC are under

development to provide more convenient implementation and operator use. The proposed AutoMQA system also shows strong potential for automation of the other QA procedures, such as couch translations or rotations.

TABLE 6. Mechanical QA items (TG-142) list identifying availability with AutoMQA system.

Procedure	Tolerance	AutoMQA precision
Available		
Gantry rotation angle indicator	1.0°	0.06°
Collimator rotation angle indicator	1.0°	0.06°
Jaw position indicator	1 mm	0.27 mm
Cross-hair centering	1 mm	0.27 mm
Optical distance indicator (ODI)	1 mm	0.27 mm
Not available		
Light/radiation field coincidence	1 mm	N/A
Treatment couch position indicators	2 mm/1.0°	N/A
Localizing lasers	1 mm	N/A

5. Conclusions

Most mechanical QA items recommended by AAPM TG142 can be tested by the proposed AutoMQA system with acceptable accuracy and precision. AutoMQA provides the opportunity for independent online monitoring of mechanical accuracy, and could eventually eliminate error prone and time consuming manual QA procedures.

Chapter II. Real-time Optical Image-based Monitoring (ROIM) System for Radiotherapy

Abstract

PURPOSE: To implement the in-house real-time optical image-based monitoring (ROIM) system for extremity soft tissue sarcoma (STS) patients treated with postoperative 3D conformal radiation therapy (3D-CRT) and test the clinical efficacy of the ROIM system as an auxiliary or alternative means of image guided radiation therapy (RT) for this patient population.

METHODS: A stereo camera system consisting of two CCD cameras was mounted on the interior wall of the treatment room. The stereo camera system was calibrated to reconstruct 3D coordinates of multiple markers with respect to the iso-center, using the direct linear transform (DLT) algorithm. Infra-red (IR) reflecting markers were attached on the patient's skin and then set up as usual. Patient real time position was acquired through the stereo camera system by detecting the IR marker positions. Detection errors with respect to the reference positions of planned CT images were calculated with six degrees of freedom (DOF) by a rigid body registration technique. To test clinical feasibility of this system, inter and intra-fractional motions for five extremity STS patients (1 upper, 4 lower) receiving 3D-CRT were measured using the ROIM system. To compare with X-ray image based monitoring, pre and post-treatment cone beam computed tomography (CBCT) scans were performed once per week and registered with the planned CT image. Where CBCT scan was not feasible due large couch shifts, Anterior-Posterior (AP) and Left-Right (LR) on-board imager (OBI) images were acquired. Quantitative comparison

was performed by calculating mutual information (MI) between the CBCT images corrected by motion data and the planned CT image.

RESULTS: System accuracy and precision to measure translational and rotational motion were 0.3 ± 0.2 mm and 0.11 ± 0.06°, respectively. The mean absolute error (MAE) for inter-fractional motion was 2.6 ± 1.4 mm LR, 2.8 ± 1.1 mm SI, 2.0 ± 1.3 mm AP, 1.8 ± 0.3° pitch, 1.3 ± 0.6° yaw, and 1.3 ± 1.1° roll; and the MAE for intra-fractional motion was 0.8 ± 1.4 mm LR, 0.6 ± 1.1 mm SI, and 0.4 ± 0.7 mm AP, 0.7 ± 0.8° pitch, 0.6 ± 1.2° yaw, and 1.1 ± 0.9° roll. Average MI values were 0.89 for CBCT-based correction and 0.91 for ROIM-based correction.

CONCLUSIONS: We demonstrated clinical feasibility of the proposed ROIM system to monitor daily extremity STS patient's motion in real-time with acceptable accuracy and precision. Thus, the ROIM system can be used as an auxiliary or alternative means of image guided RT for this patient population.

1. Introduction

Recent technological advances for dynamic beam delivery and dose conformation have allowed increasing clinical applications of high precision radiotherapy. However, high precision radiotherapy requires consistent patient immobilization to minimize the geometric uncertainty while maximizing exclusion of normal tissue from the irradiated volume [37]. However, it is difficult to draw consistent conclusions on the accuracy of localization and immobilization in conventional radiotherapy [38,39]. Several invasive (e.g. fixed pin systems) and noninvasive (e.g. thermoplastic or vacuum formed cradle) systems for immobilization have been introduced [40]. Although these systems seem to work well in the clinic [3], they may, nevertheless, allow significant daily variation in target alignment. Karger *et al*. showed that immobilization with a thermoplastic mold was not sufficient for high precision radiotherapy without additional image guided techniques. The mean length of the displacement vector using the thermoplastic mold was 4.72 ± 1.74 mm and 7.26 ± 4.45 mm in the intracranial and neck regions, respectively [38]. Hong *et al*. assessed localization of twenty H&N cancer patients with conventional H&N masking and laser alignment for daily positioning. The mean setup error in any single dimension was 3.33 mm. However, when all 6 degrees of freedom (DOF) were accounted for, using an optically guided patient localization system, the mean composite vector offset was 6.97 ± 3.63 mm [41].

X-ray based guidance systems (e.g. EPID or CBCT) have risk for excessive radiation exposure with no feasible way to monitor patients during the

treatment [42]. Optical guided systems have been developed to help avoid excessive EPID and CBCT radiation exposure and satisfy efficiency in the busy clinic [43–47]. Li *et al*. developed a 3D surface guided system for fractionated stereotactic radiotherapy, which has acceptable accuracy and precision of < 1 mm [42].

The AlignRT® (Vision RT Ltd., London, UK) system also uses a 3D surface guided method. However, to reconstruct the patient's skin surface, part of the immobilization device must be modified, and setup accuracy strongly depends on the region of interest (ROI) selected for the surface reconstruction [48]. Frameless SonArray™ integrated with RadioCameras™ (FSA, Zmed/Varian Inc., Ashland, MA), another optical image guided system, uses IR markers and is also available for localization. However, it is only applicable when the patient collaborates and keeps pressure on the block during the entire treatment session [45,49].

The other commercially available system, ExacTrac® (BrainLAB, Heimstetten, Germany) system tracks IR markers during treatment. Attaching IR markers to the patient's skin for tracking is only used in treatment of intra-abdominal organs or prostate, but for other cases utilizing immobilization devices it is relatively common to place IR markers or IR marker plates on the immobilization device. Thus, it can only localize the immobilization device, rather than patient motion directly [49–51].

To address the drawbacks of conventional X-ray and commercial optical image guided systems, we propose a real time optical image based monitoring (ROIM) system for managing inter and intra-fractional set-up errors for cancer

patients by tracking IR external markers. The developed system was able to determine 3D positions of external markers in the treatment coordinates using a pair of charged coupled device (CCD) cameras and a specific calibration procedure. We validated the system accuracy and consistency prior to clinical implementation.

Clinical data from several studies support the combination of radiation therapy (RT) with surgery for treatment of soft tissue sarcoma (STS) [52–56]. Conformal RT for extremity STS patients precisely delivers a high dose to the target volume while allowing successful limb preservation, leading to good local control with minimum toxicity [57–60].

However, high precision RT requires consistent patient localization to minimize geometric uncertainty [2,61], but position reproducibility of extremity STS patients can be challenging. Some immobilization devices (e.g. Polystyrene or vacuum filled cradles) have been introduced because of the relatively low incidence of STS. Those devices provide lateral extremity stability, but are prone to misalignment in superior-inferior (SI) and anterior-posterior (AP) directions [62]. Dickie *et al.,* designed a customized device that improved positioning uncertainty in all directions [62]. A subsequent study measured the inter- and intra-fractional error with the custom immobilization device [63] and showed it was still prone to individual geometric variation of the treatment region. Moreover, extremity lesions are often bulky and longitudinally developed, which are prone to rotational errors. Thus, 3D image guidance is required for this patient population.

3D image guidance though X-ray imaging is available in the form of cone beam computed tomography (CBCT). However, daily CBCT imaging is impractical due to excessive radiation exposure (3 cGy per acquisition) [64] and infeasible for real time monitoring during the treatment. Keall *et al.* developed an X-ray based real time monitoring system, kilovoltage intra-fraction monitoring (KIM). However, this has not been commercialized and also risks additional radiation exposure [65]. To address these drawbacks, optical imaging enabling real time noninvasive patient position monitoring is essential.

This study describes the application of an in-house ROIM system, detecting infra-red (IR) markers, to measure daily inter- and intra-fractional motion of both upper and lower extremity STS subjects treated with 3D conformal radiation therapy (3D-CRT). The efficacy of optical imaging as an auxiliary or alternative means of image guided RT is discussed through quantitative comparison with motion data measured by CBCT. To the best of our knowledge, there are no published data of quantitative comparison of motion detection between optical and X-ray based monitoring for this patient population.

2. Material and Methods

2.A. System description

In our ROIM system, patient localization was accomplished through detection of three IR reflector markers (ScotchliteTM 3000X, 3M, MN, USA). Those were attached to the selected points on patient's skin. The 3 dimensional locations of the markers were imaged by the stereo camera system that is mounted on the wall of the treatment room. Detailed descriptions of the stereo camera system and the calibration method are given in Sec. 2.B. The reference coordinate of IR reflector markers were obtained from patient's planning CT images, i.e., treatment coordinate system. The positions of three IR reflector markers were registered with respect to the reference coordinate. With this registration, the system allowed determination of the rigid body position and misalignment in terms of both translation and rotation. Details of the registration method are given in Sec. 2.B.e. The determined positional misalignment was compared with that derived from the X-ray images (CBCT). A schematic illustration of the developed ROIM system is shown in Figure 14.

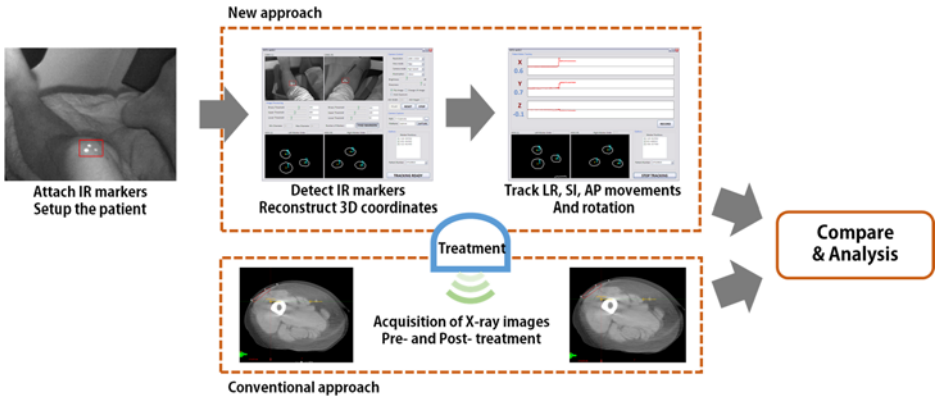

Figure 14. A schematic of the developed ROIM system. Three IR markers were attached on the skin of the patient. Reference positions of markers were calculated by RTPS and real-time positions of the markers with respect to iso-center of treatment room were calculated by stereo camera system installed on the inferior wall of treatment room. Then the positions of three IR reflector markers were registered with respect to the reference coordinate. The derived positional error was compared with that derived from the X-ray images (CBCT).

2.B. Infra-red stereo camera system

2.B.a. Hardware

The ROIM system was developed to monitor patients with various tumor locations. The hardware of the system consists of two CCD cameras (AV5115dn, Arecont Vision, USA) with power over Ethernet (POE) interface, IR filters (B+W092, Bad Kreuznach, Schneider, Germany), two IR LEDs and a PC with a CPU clock of 2.8 GHz. A railed frame was fabricated to accurately adjust the baseline between the two cameras that can affect accuracy in stereo camera calibration [66]. The frame assembled with the cameras, IR filters and IR LEDs was installed on the inferior wall of treatment room (see Figure 15).

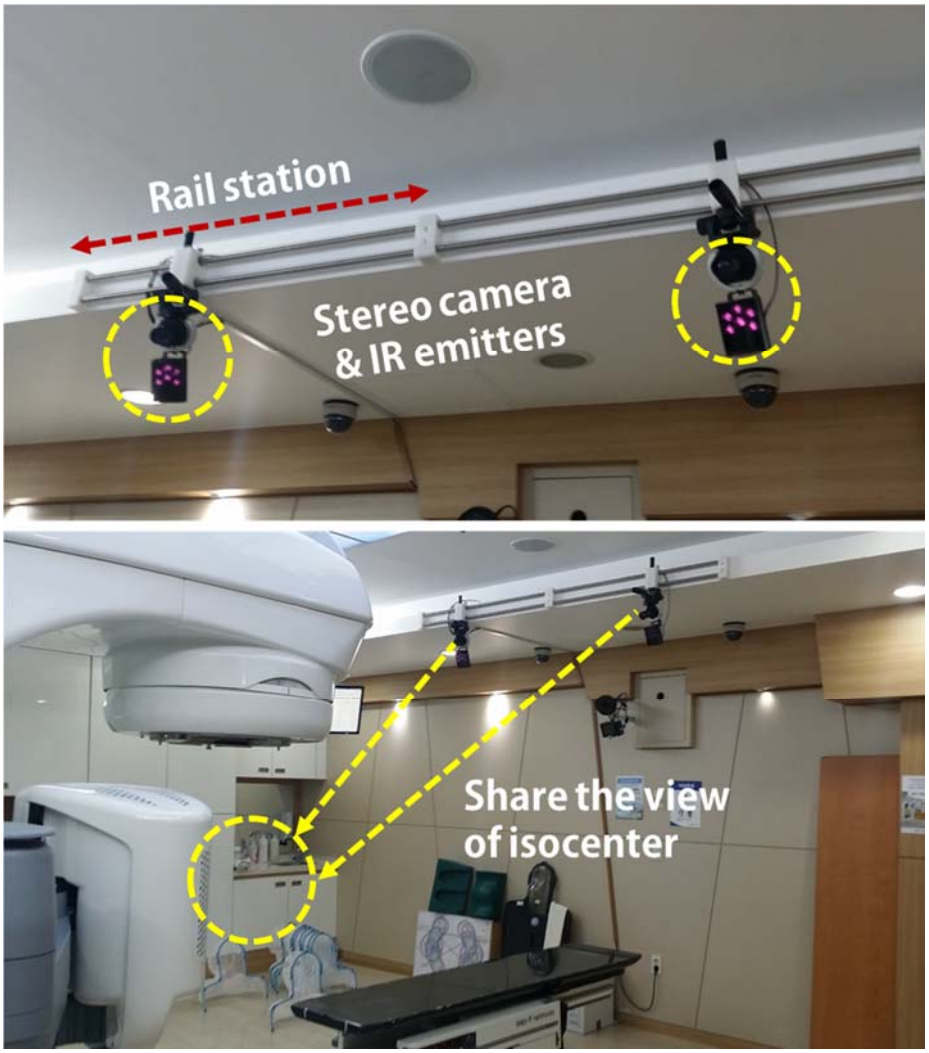

Figure 15. The stereo camera system mounted on the inferior wall of treatment room. The CCD cameras with IR filters receive the IR signals from the IR LEDs and interfaced to a PC. A railed frame was fabricated to accurately adjust the baseline between the two cameras.

2.B.b. Stereo camera calibration

In order to extract metric information from 2D images, it is necessary to calibrate the camera. Stereo-camera calibration was performed with a checkerboard template and free software (Camera Calibration Toolbox, Imperial College, London, UK). The calibration procedures followed Zhang's method [67, 68]. We acquired ten images of the checkerboard template under different poses by moving the template. Each square on the template was 28 mm × 28 mm. Then we detected the feature points in the images and estimated the intrinsic and extrinsic parameters using the direct linear transform (DLT) method [69].

The DLT method uses a set of feature points whose object space coordinates are already known. This was the reason we used checkerboard template in this camera calibration. The essential issue here is to calculate the mapping between the 2D image coordinates system (ICS, x_i) and the 3D real coordinates system (RCS, X_i). For this correspondence the mapping take the form of a 3 × 4 projection matrix (P) such that $x_i = PX_i$ for all i. Finally, the projection matrix P includes intrinsic and extrinsic parameters as follows:

$$P_{3\times4} = I\left[R \mid T\right] = \begin{bmatrix} \alpha_x & 0 & x_0 \\ 0 & \alpha_y & y_0 \\ 0 & 0 & 1 \end{bmatrix} \left[R \mid T\right] \qquad (1)$$

I: intrinsic parameter matrix (a_x, a_y: focal length, x_0, y_0: principal point)

R: Rotational matrix (3 × 3)

T: Translational matrix (3 × 1)

2.B.c. 3D reconstruction

The stereo camera system was calibrated to reconstruct 3D coordinates using the DLT algorithm as described in the previous section. The origin of the 3D world coordinate system was the iso-center of treatment room. The 3D reconstruction was done by using the linear triangulation method [70].

For each input image, there is a set of measured data, i.e., $x = PX$, $x' = P'X$ where x is the 2D image coordinates of a real point, x' is the same point projected onto the image coordinates of the other camera. X represents the 3D real coordinates that we are attempting to recover. These two equations can be combined into a form $AX = 0$, which is a linear equation of X. The homogeneous scale factor is eliminated by a cross-product to give three equations for each image point in the system. As an example the equation derived for a point in the first image would be given as $x \times (PX) = 0$. Expanded, this gives the following set of three equations:

$$\begin{aligned} x(p^{3T}X) - (p^{1T}X) &= 0 \\ y(p^{3T}X) - (p^{2T}X) &= 0 \\ x(p^{2T}X) - (p^{1T}X) &= 0 \end{aligned} \tag{2}$$

Combining equations from both cameras to produce an equation in the form $AX = 0$ gives us:

$$A = \begin{bmatrix} xp^{3T} - p^{1T} \\ yp^{3T} - p^{2T} \\ x'p'^{3T} - p'^{1T} \\ y'p'^{3T} - p'^{2T} \end{bmatrix} \tag{3}$$

Solving for A using singular value decomposition (SVD) allows us to estimate the value of X and thus the 3D coordinates of any point for which we know the image coordinates from two cameras for which the projection matrix

has already been determined [69].

2.B.d. IR marker detection

To assume the most challenging situation of determine marker positions, we considered head and neck case with thermoplastic mask as an immobilization device. Thus, we used a head phantom (RANDO® Phantom, The Phantom Laboratory, NY, USA) and thermoplastic mask. The markers were attached on the face of a head phantom and then the phantom was immobilized by thermoplastic mask.

The real-time position of the phantom was acquired, by detecting the IR markers with the stereo camera system. All of the markers were clearly detected despite their positions being behind the thermoplastic mask.

Detection of the IR markers was done with image processing described behind. First, we simply got binary images with a threshold. Then the edges of the markers were detected by the Canny method [71]. Finally, the current positions of the markers were calculated by determining the centroid of each edge (see Figure 16).

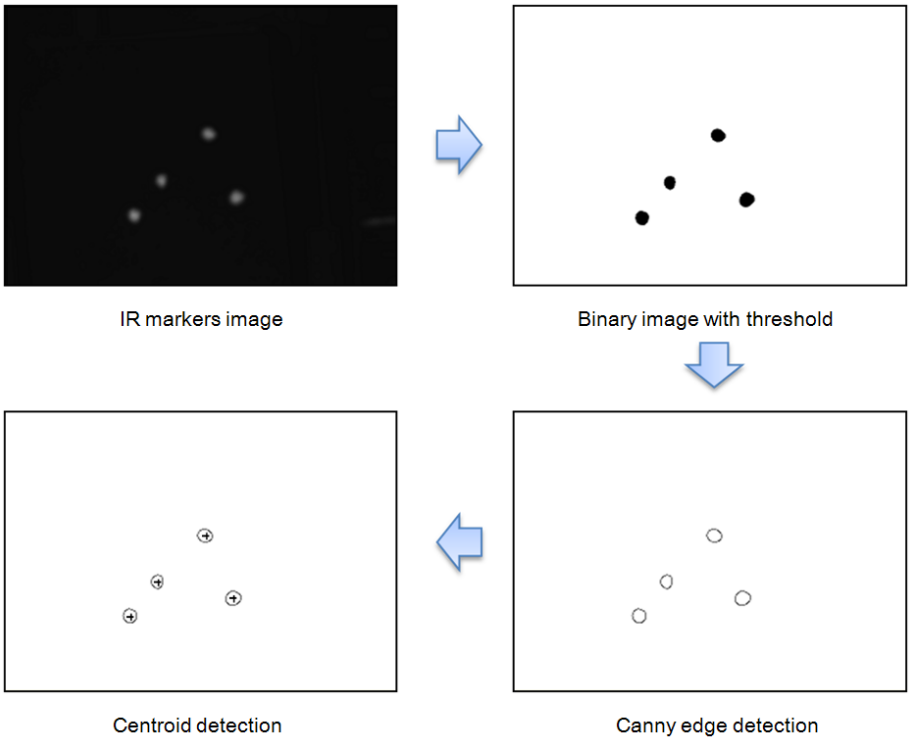

Figure 16. A flow diagram of image processing for IR marker detection: raw IR markers image (top left), binary image with a threshold (top right), detected edges of the markers by the Canny method (bottom right), determined the centroid of each edge (bottom left).

2.B.e. Registration with planning CT images

Three markers were attached on the skin of the phantom. Then the phantom was immobilized by thermoplastic mask before taking CT scans for treatment planning.

With the planning CT images, the positions of three markers with respect to the iso-center of treatment room can be calculated by the radiation treatment planning system (Eclipse, Varian Medical Systems, CA, USA). In the treatment room, the real-time position of the phantom was acquired, by detecting the IR markers. The two cameras were placed properly enough to secure a full view of all three markers.

These three IR markers were registered with the positions of corresponding three markers from the CT images and then 6-DOF correction between the reference and the acquired positions was calculated according to the Gauss-Newton method [43, 72].

Denoting $E(\vec{q})$ as an objective function to be minimized, it is described as least squares for residual errors between the current positions of markers and the reference positions of markers. This is expressed as follows:

$$E(\vec{q}) = \sum_{i=1}^{9} \mathbf{b}_i^2, \qquad \mathbf{b} = \begin{bmatrix} b_1 \\ \dots \\ b_9 \end{bmatrix} = \begin{bmatrix} x_1 - x_1' \\ x_2 - x_2' \\ x_3 - x_3' \\ \dots \\ z_3 - z_3' \end{bmatrix} \tag{4}$$

(x_n, y_n, z_n), n = 1, 2, 3 : the reference position of three markers

(x'_n, y'_n, z'_n), n = 1, 2, 3 : the current position of three markers

Then, the objective function can be minimized through iteration. In each iteration, parameter $\vec{q}$ is updated as follows:

$$\vec{q}(n+1) = \vec{q}(n) - (\mathbf{A}^T\mathbf{A})^{-1}\mathbf{A}^T\mathbf{b} \tag{5}$$

$$\mathbf{A} = \begin{bmatrix} \frac{\partial b_1(\vec{q})}{\partial q_1} & \cdots & \frac{\partial b_6(\vec{q})}{\partial q_1} \\ \vdots & \ddots & \vdots \\ \frac{\partial b_1(\vec{q})}{\partial q_6} & \cdots & \frac{\partial b_6(\vec{q})}{\partial q_6} \end{bmatrix} \tag{6}$$

This iteration is terminated whenever it meets the given condition as follows:

$$E(\vec{q}) < \varepsilon (= 0.00001) \tag{7}$$

When this iteration is terminated, the parameter $\vec{q}$ corresponds to translational and rotational vectors of misalignment. This informs us of 6-DOF correction of the phantom in the treatment room.

2.C. System evaluation

The system was tested against optical translation and rotation stages to determine the accuracy and precision prior to the clinical application (Figure 17). Three IR markers were attached to the template on the optical translation and rotation stages (ST1-418-B4, Sciencetown, Republic of Korea). Thereafter, we intentionally moved the markers with 10 known translations and rotations along the each axes by using optical translation and rotation stages, respectively. We measured deviations between current positions of the markers and their known reference positions in terms of mean absolute error (MAE). Each of test set was repeated five times to confirm the reproducibility of the system.

In order to verify that brightness and contrast of the CCD cameras didn't affect detection consistency of the markers, we measured deviations among the real time positions of markers with different setups for brightness and contrast in each five second interval.

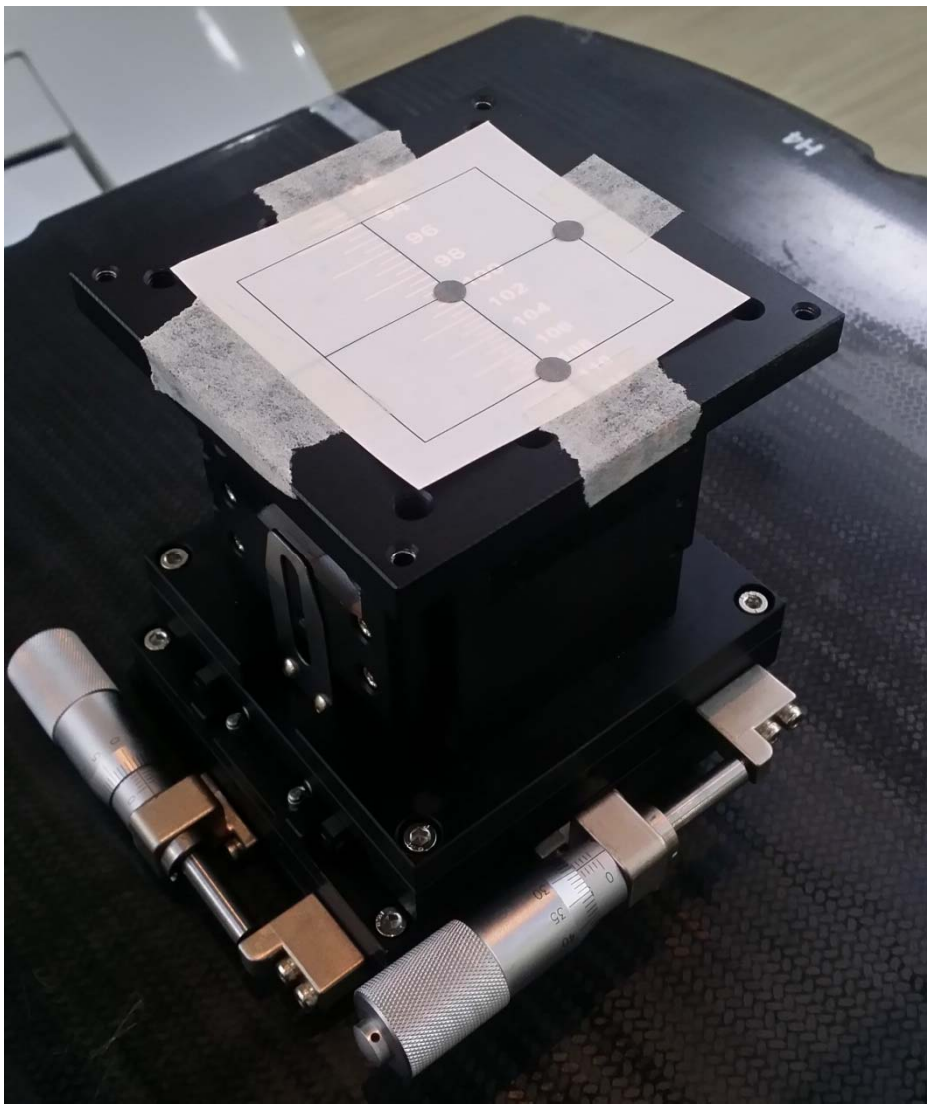

Figure 17. Three markers were attached to the template on the optical translation stage.

TABLE 7. The test sets with known translations.

(mm)	LAT	SI	AP	LAT+SI	LAT+AP	SI+AP	ALL
1	-3.0	-3.0	-3.0	-3.0, -3.0	-3.0, -3.0	-3.0, -3.0	+3.0, -3.0, +3.0
2	-5.0	-5.0	-5.0	+3.0, +3.0	+3.0, +3.0	+3.0, +3.0	-3.0, -3.0, +3.0
3	-5.2	-5.2	-5.2	+5.0, +5.0	+5.0, +5.0	+5.0, +5.0	+5.0, -5.0, -5.0
4	-5.5	-5.5	-5.5	-5.0, +5.0	-5.0, +5.0	-5.0, +5.0	-5.0, +5.0, +5.0
5	-7.0	-7.0	-7.0	-5.2, +5.0	-5.2, +5.0	-5.2, +5.0	-5.2, +5.0, +5.0
6	+3.0	+3.0	+3.0	-5.5, +5.2	-5.5, +5.2	-5.5, +5.2	-5.5, -5.2, +5.2
7	+5.0	+5.0	+5.0	-7.0, -5.2	-7.0, -5.2	-7.0, -5.2	-7.0. -5.2, -5.2
8	+5.2	+5.2	+5.2	-7.0, -5.5	-7.0, -5.5	-7.0, -5.5	-7.0, -5.5, -5.5
9	+5.5	+5.5	+5.5	+7.0, -5.5	+7.0, -5.5	+7.0, -5.5	+7.0, -5.5, -7.0
10	+7.0	+7.0	+7.0	+7.0, -7.0	+7.0, -7.0	+7.0, -7.0	+7.0, -7.0, +7.0

2.D. Clinical application: Extremity soft tissue sarcoma patients

This prospective research was approved by an institutional research ethics board (IRB-1503-108-657) in our institution. Five extremity STS patients receiving postoperative 3D-CRT (4 lower, 1 upper) were treated during the study timeframe of September 2015 to April 2016. We excluded patients from the study whose treatment plan included bolus compensation.

In this study, translational and rotational errors are defined as the deviations between the image acquired by daily CBCT or ROIM system and that from the planning CT of a region of interest (ROI) with respect to a reference point determined by three radiopaque markers on the patient's skin.

2.D.a. Measurement of inter-fractional motion

All patients were immobilized by vacuum-filled cradle and localized with room lasers. To derive inter-fractional motion, pre-treatment CBCT images were acquired once per week (total 5 scans per each patients). A region of interest (ROI) was set to encompass the planning target volume (PTV) and bony landmarks. The pre-treatment CBCT image was rigidly registered to the planning CT image within this ROI. If the positional correction was needed (displacement exceeds 3 mm in each direction), the subsequent CBCT image was acquired for setup confirmation. For two patients (1 upper, 1 lower), we acquired two orthogonal on-board imager (OBI) images instead of the CBCT

image due to the large lateral couch shift.

The inter-fractional motion monitoring with ROIM system was done for every fraction. The reference positions of three IR markers were tattooed during the CT simulation process and their coordinates were identified by the locations of radio-opaque markers from the planning CT image. Three IR markers were attached on the tattooed position prior to the treatment and the ROIM system reconstructed three marker coordinates with respect to the iso-center. Inter-fractional motion was calculated in each directions using registration of current marker positions to their reference positions. For the upper extremity case, the PTV included both arm and shoulder region. Thus we acquired each inter-fractional motion of those two region. We derived MAE and standard deviation (SD) of measured inter-fractional motions.

2.D.b. Measurement of intra-fractional motion

Intrafractional motion was assessed using the ROIM system combined with pre- and post-treatment CBCT scans performed once per week (five times in total per patient). This ROIM system provides real-time tracking of the patient's position. Optical tracking was initiated immediately before the delivery of the first RT beam and was terminated following delivery of the final beam. The mean maximum relative displacement of all markers was calculated in the LR, SI, and AP dimensions and random and systematic errors were calculated. In addition to the tracking with ROIM system, the positional displacement during treatment was estimated using the calculated deviation between the pre-

treatment CBCT and a post-treatment CBCT acquired immediately following the delivery of the radiotherapy fraction. Automated gray value matching with visual confirmation in 3D was utilized for registration purposes to minimize inter-observer error. The positional difference between the pre-treatment CBCT image and post-treatment CBCT image was calculated by using Eclipse treatment planning software and compared to the derived intra-fractional error by using the ROIM system (Figure 18). The derived positional deviations were displayed in real-time during the treatment (Figure 19).

2.D.c. Multiple region of interest analysis

In the case of Patient 3 (upper extremity), the treatment region shown a non-rigidity between the arm structure and the shoulder structure. This may introduce extra setup deviations, due to the inability of the setup correction for multiple region by X-ray imaging system. A simple translational correction cannot compensate the relative motion between the each structures [73].

In order to improve on the drawbacks of this conventional setup correction policy, we investigated setup uncertainties, including translations and rotations, for two individual structures in the extremity region by separately registering these two structures in the daily image acquired by the ROIM system to their corresponding positions in the reference planning CT image, independently.

2.D.d. Comparison

The goal of this comparison was to test whether the motion correction with

the data acquired by ROIM system is sufficient or not. A quantitative analysis was performed by observing the mutual information (MI) between the corrected online CBCT images and the planning CT image. MI as an index of the similarity measure between multimodality images was introduced by Viola *et al.* [74] and Maes *et al.* [75]. Cross correlation assumes merely a linear relationship between two sets of data (directly compares pixel values for each coordinate). Whereas mutual information assumes that one value from one dataset informs about the value of the other dataset. The problem to solve with mutual information is a registration of two images of different modalities (CBCT and CT). Therefore, mutual information is still a useful criterion for aligning the images, but cross correlation is not.

MI is consisted of joint entropy and the individual entropy of two images. The joint entropy is minimized when there exist a perfect one-to-one mapping between the values in two images. For given image A and B, the joint entropy H(A, B) can be derived as follow:

$$H(\mathrm{A},\mathrm{B}) = -\sum_{a,b} p_{AB}(a,b)\log p_{AB}(a,b)$$

where p_{AB} is a joint probability distribution of the intensity values associated with images A and B. This joint entropy H(A, B) is minimized when there exist a perfect one-to-one mapping between the values in the image A and B. Thus, mutual information can be calculated as below:

$$MI = H(A) + H(B) - H(A,B)$$

where the individual entropy $H(\mathrm{X}) = -\sum_x p_X(x)\log p_X(x)$.

We compared MAEs of MIs between the following images and the planning CT image, respectively: (1) the online CBCT image corrected with only translational motion acquired by CBCT ($CBCT_{w/o\ rot}$), (2) the online CBCT image corrected with translational and rotational motions acquired by CBCT ($CBCT_{w/\ rot}$), (3) the online CBCT image corrected with only translational motion acquired by ROIM system ($ROIM_{w/o\ rot}$), and (4) the online CBCT image corrected with translational and rotational corrections acquired by ROIM system ($ROIM_{w/\ rot}$). For this comparison, selected ROI was a quadrilateral with a 3 mm margin from a quadrilateral circumscribed about a PTV. The calculated MI was normalized to the maximum bounded value.

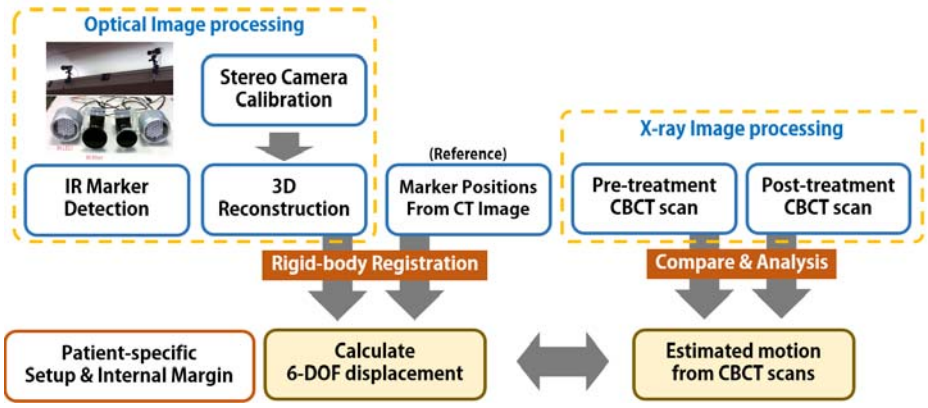

Figure 18. A description of clinical application of ROIM system. Each interfractional and intrafractional errors was derived from ROIM system and CBCT scans. Comparison between the calculated 6-DOF displacement from ROIM system and the estimated motion from CBCT scans were done.

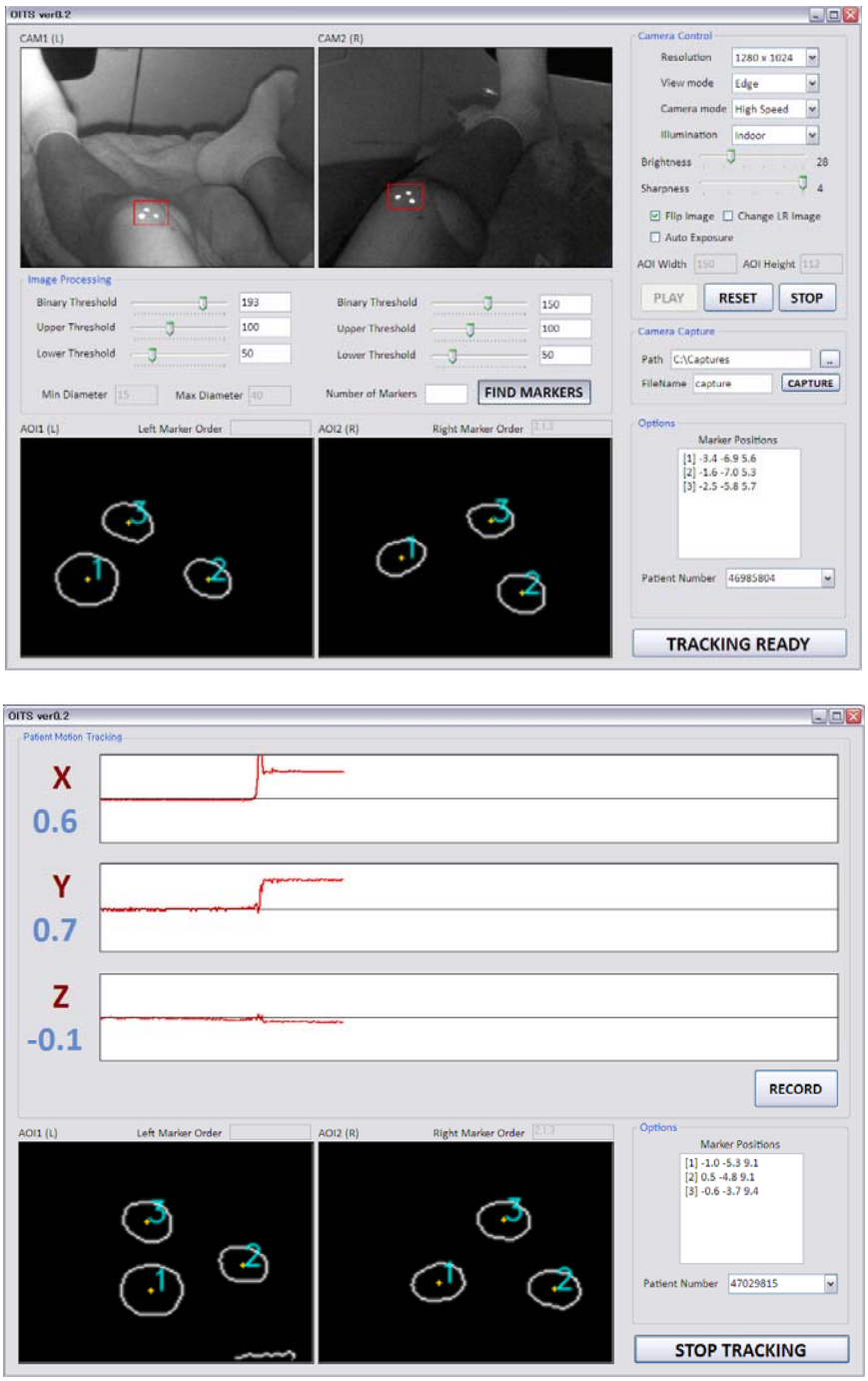

Figure 19. Screen shots of ROIM system. The derived positional deviations were displayed in real-time.

3. Results

3.A. ROIM system evaluation

The MAE and SD of the current markers' translational error from the reference positions from the planning CT images were 0.3 mm and 0.2 mm, respectively. In each direction, the MAEs were 0.3 ± 0.2 mm, 0.3 mm ± 0.2 mm, and 0.2 mm ± 0.1 mm for the left-right (LR), SI, AP direction, respectively. The MAEs of each measured rotational errors were 0.11° ± 0.06°, 0.14° ± 0.05°, and 0.10° ± 0.07° for roll, pitch, and yaw axis, respectively. The applied 6-DOF registrations determined the maximum deviations from the reference to be less than 1 mm and 0.3° for the known translations and the rotations, respectively. Thus, the accuracy and precision of the ROIM system would be sufficient to assess motion

The results for system consistency of the marker detection are shown in TABLE 8. The mean deviation and standard deviation of the markers' position with brightness and contrast variations were 0.17 mm and 0.24 mm, respectively.

TABLE 8. System consistency: mean absolute errors of detected displacements of the IR markers with various brightness and contrast condition in each direction

Brightness/Contrast	LAT (mm)	LNG(mm)	AP (mm)	TOT (mm)
62/62 (L_CAM) 30/30 (R_CAM)	0.06±0.13	0.11±0.22	0.18±0.37	0.12±0.24
299/299 (L_CAM) 105/105 (R_CAM)	0.12±0.13	0.32±0.32	0.33±0.32	0.26±0.26
336/324 (L_CAM.) 223/234 (R_CAM)	0.06±0.10	0.21±0.34	0.14±0.19	0.13±0.22
Mean ± SD	0.08±0.11	0.21±0.34	0.14±0.19	0.17±0.24
Max (abs.)	0.27	0.72	0.75	N/A

Abbreviations: L_CAM = left camera; R_CAM = right camera; SD = standard deviation; LAT = lateral direction; LNG = longitudinal direction; AP = anteroposterior direction; TOT = mean absolute errors for all direction

Notes: Maximum value is calculated in absolute terms

3.B. Clinical application

3.B.a. Interfractional error

We measured the interfractional motion, along with rotational evaluation, for a subgroup of two extremity sarcoma patients using online CBCT images acquired before positional correction, retrospectively. The initial setup result shows that patient skin adjacent with the tattooed at simulation process was well matched with the body surface in planning CT image, however, there exists severe displacements of the other parts of the treatment region. In practice, patients were usually set up only with translational correction along the axis with couch movements, this results in misalignment of the treatment region mainly due to the rotational shift even with the vacuum cradle immobilization.

The rotation correction is possible with CBCT technically, however, it is not easy in practice. To do that, therapists should manually re-setup the patient which may be cause of the other misposition errors and a series of CBCT scan is not avoidable which causes excessive radiation dose to the patient (up to 3 cGy/acquisition for soft tissue). Thus the optical image-based guidance system for patient setup is highly needed.

For lower extremity patients, the MAEs and SDs of the inter-fractional motion derived by ROIM system in each direction were 2.6 mm ± 1.4 mm LR, 2.8 mm ± 1.1 mm SI, and 2.0 mm ± 1.3 mm AP. The rotational motions in terms of MAEs and SDs were 1.8° ± 0.3°, 1.3° ± 0.6°, and 1.3 ° ± 1.1° for pitch, yaw, and roll rotational axis, respectively. The setup errors were evenly distributed in all direction.

For upper extremity patient, the inter-fractional motions in terms of MAE were 3.0 mm ± 0.6 mm LR, 2.7 mm ± 0.6 mm SI, and 1.0 ± 0.4 mm AP for arm structure, and 1.4 mm ± 0.2 mm LR, 1.1 ± 0.1 mm SI, and 0.2 ± 0.0 mm AP for shoulder structure. For rotational errors in each axis were 2.1° ± 0.3° pitch, 1.2° ± 0.6° yaw, and 0.9° ± 0.4° roll for arm structure, and 0.2° ± 0.1° pitch, 1.5° ± 0.8° yaw, and 1.5° ± 0.6° roll for shoulder structure.

TABLE 9 summarizes the overall inter-fractional motions derived from the CBCT and the ROIM system. Translational motions acquired by ROIM system did not significantly deviate from those by CBCT ($P < .10$), whereas the rotational motions did not showed consistent results each other.

Figure 20 shows an example of the daily CBCT image-reference planning CT image registration result. Initial setup showed severe discrepancy of surface and soft tissue matching between the two images. When rotation correction was applied, two images were matched better than the case with only translation correction was applied.

Figure 21 and Figure 22 shows a trend graph and 3D distribution plot of the interfractional error for Lt. thigh patient and Lt. knee patient, respectively..

TABLE 9. The comparison of inter-fractional motions derived from the CBCT and the ROIM system. For patient 3 and 5, we acquired two orthogonal OBI images instead of CBCT images due to the large couch shift (thus rotational motions couldn't be assessed).

Patient #		1	2	3	4	5	
						Arm	Shoulder
Translational (mm)							
LR	ROIMS	2.8 ± 1.0	3.3 ± 1.0	4.0 ± 1.6	3.4 ± 1.3	3.0 ± 0.6	1.4 ± 0.2
	CBCT	2.9 ± 1.2	2.5 ± 0.7	3.2 ± 0.6	2.8 ± 1.6	2.6 ± 0.7	1.3 ± 0.6
SI	ROIMS	3.0 ± 0.8	3.4 ± 0.8	2.5 ± 1.9	2.6 ± 1.0	2.7 ± 0.6	1.1 ± 0.1
	CBCT	2.5 ± 1.5	2.6 ± 1.0	3.3 ± 2.3	2.9 ± 0.5	3.6 ± 0.9	1.4 ± 0.6
AP	ROIMS	1.5 ± 0.7	2.1 ± 1.0	1.3 ± 0.3	2.4 ± 1.5	1.0 ± 0.4	0.2 ± 0.0
	CBCT	1.1 ± 0.8	3.1 ± 2.0	1.2 ± 0.7	1.8 ± 0.9	1.5 ± 0.7	0.4 ± 0.1
3D vector	ROIMS	4.3 ± 3.1	5.2 ± 3.0	4.6 ± 2.8	3.9 ± 1.1	4.1 ± 1.0	1.7 ± 0.2
	CBCT	4.2 ± 1.4	5.1 ± 1.3	4.5 ± 1.6	3.1 ± 0.6	3.8 ± 1.2	1.3 ± 0.5
Rotational (°)							
Pitch	ROIMS	0.9 ± 0.3	1.2 ± 0.3	2.3 ± 0.2	2.2 ± 0.1	2.1 ± 0.3	0.2 ± 0.1
	CBCT	0.2 ± 0.2	1.5 ± 0.5	N/A	0.4 ± 0.2	N/A	N/A
Yaw	ROIMS	0.9 ± 0.4	0.6 ± 0.3	0.9 ± 0.5	1.5 ± 0.5	1.2 ± 0.6	1.5 ± 0.8
	CBCT	0.3 ± 0.3	1.8 ± 0.3	N/A	1.3 ± 0.2	N/A	N/A
Roll	ROIMS	1.5 ± 0.8	1.3 ± 0.7	1.2 ± 0.3	2.0 ± 1.3	0.9 ± 0.4	1.5 ± 0.6
	CBCT	0.8 ± 0.5	1.0 ± 0.8	N/A	1.5 ± 0.4	N/A	N/A

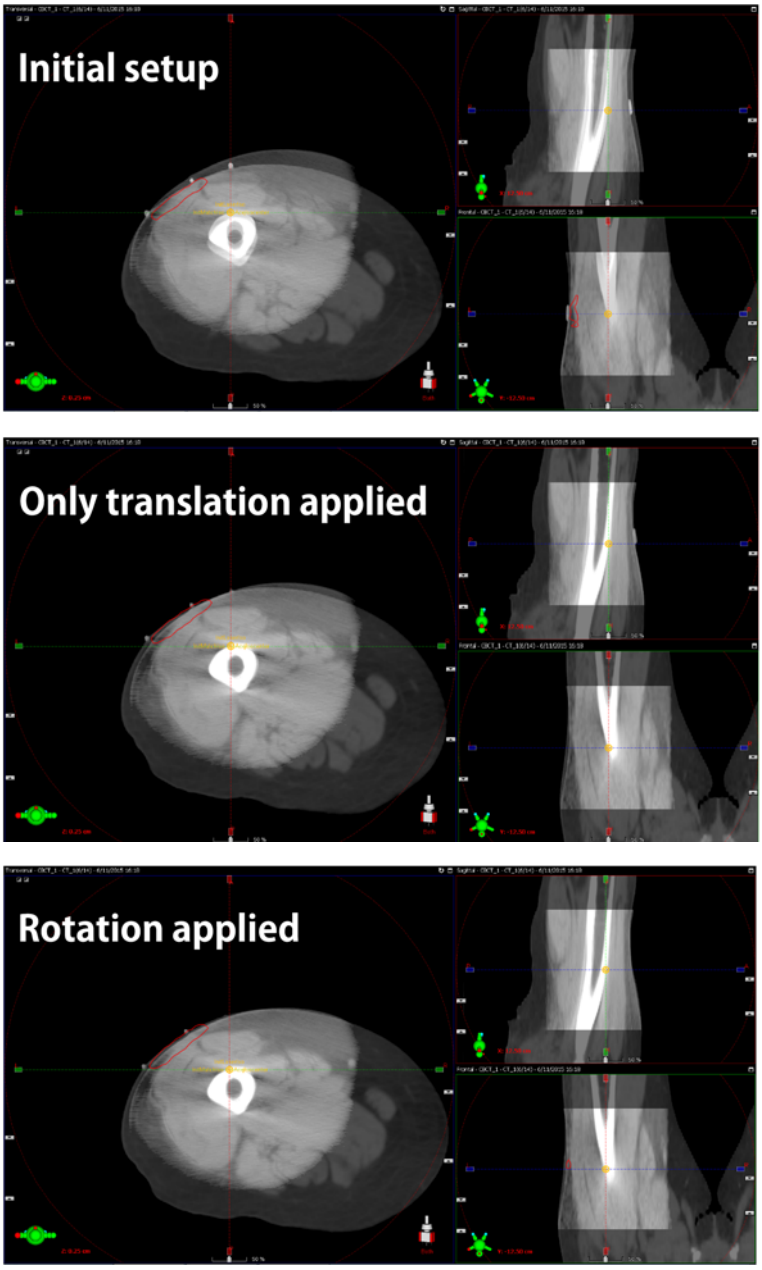

Figure 20. An example of daily CBCT-reference planning CT registration results. Initial setup shows severe discrepancy of surface and soft tissue matching between two images. When rotation correction was applied, two images were matched better than the case with only translation correction was applied.

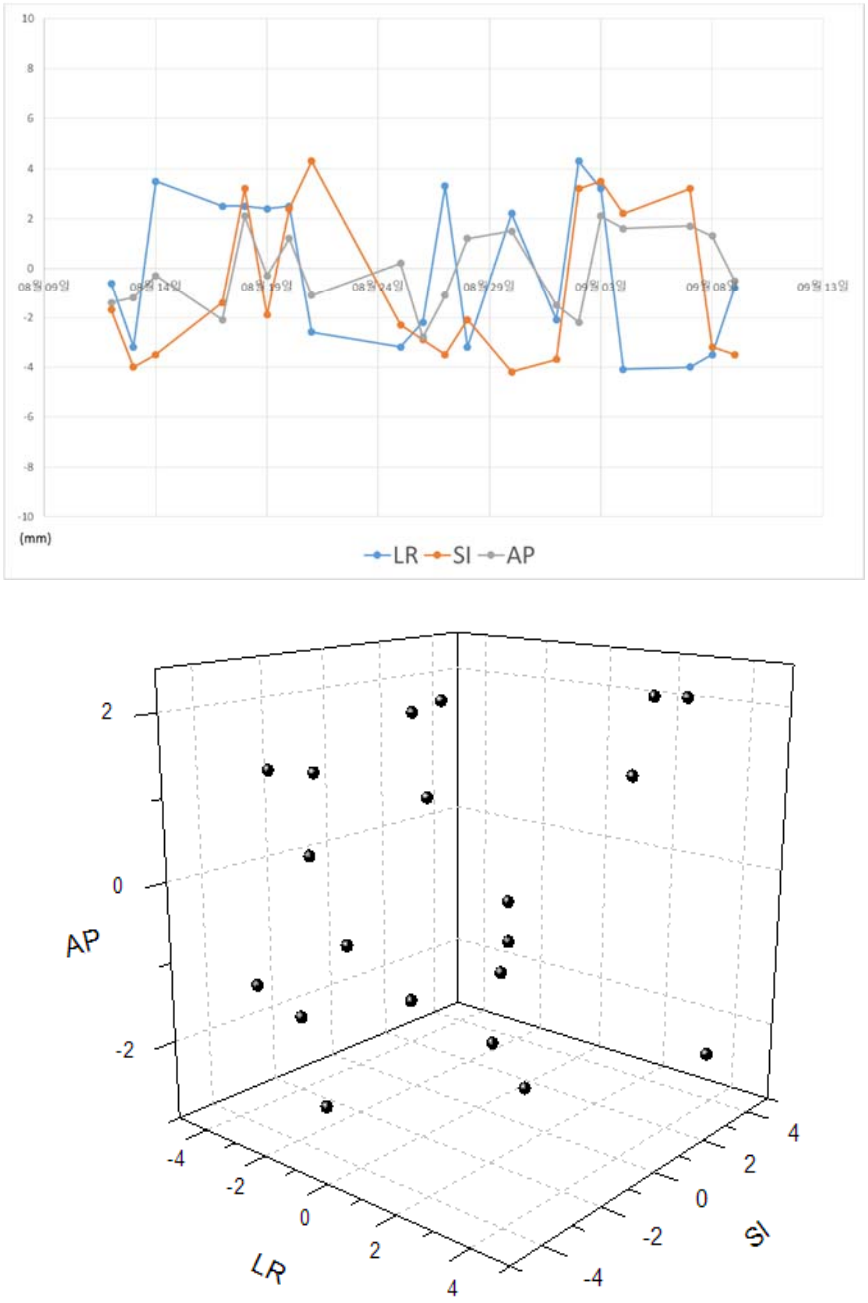

Figure 21. A trend graph and 3D distribution plot of the interfractional error for Lt. inner thigh patient.

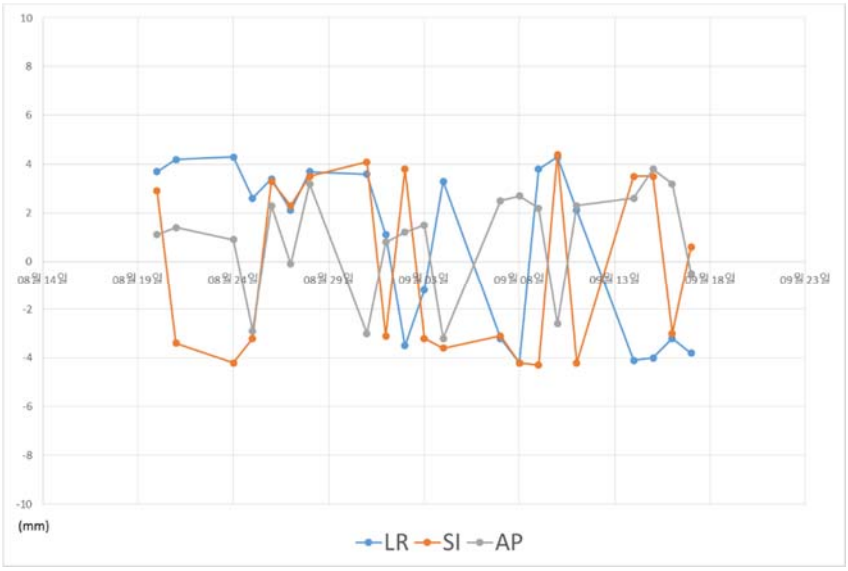

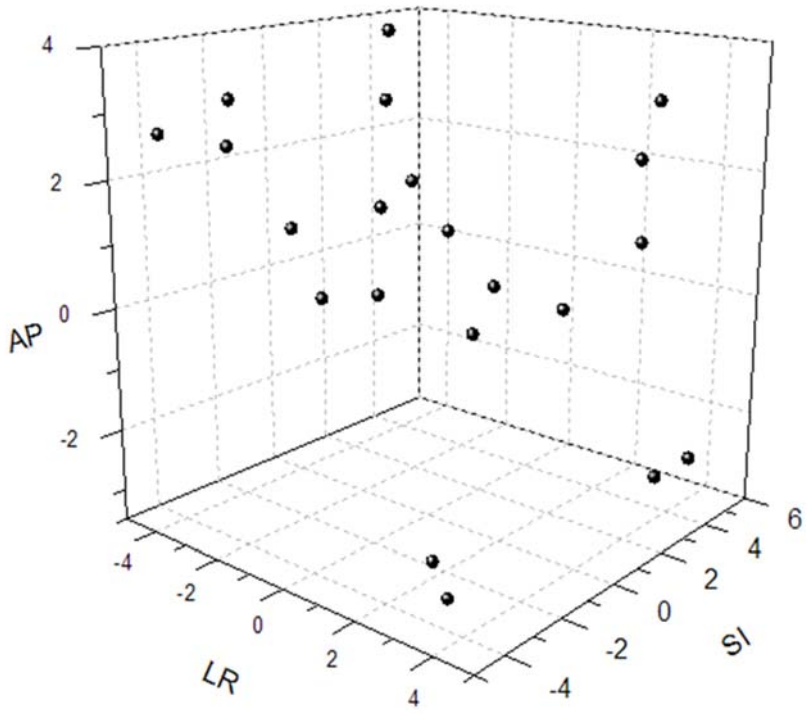

Figure 22. A trend graph and 3D distribution plot of the interfractional error for Lt. knee patient.

3.B.b. Intrafractional error

For lower extremity patients, the MAEs and SDs of the averaged intra-fractional motion derived by ROIM system in each direction were 0.8 mm ± 1.4 mm LR, 0.6 mm ± 1.1 mm SI, and 0.4 mm ± 0.7 mm AP. The averaged rotational motions in terms of MAEs and SDs were 0.7° ± 0.8°, 0.6° ± 1.2°, and 1.1° ± 0.9° for pitch, yaw, and roll rotational axis, respectively. Examples of intra-fractional motion recorded by ROIM system was shown in Figure 23 and Figure 24.

3.B.c. Multiple region of interest analysis

The interfractional errors for each structures observed by ROIM system were summarized in TABLE 10. The intrafractional errors in terms of MAE were 3.0 mm ± 0.6 mm LR, 2.7 mm ± 0.6 mm SI, and 1.0 ± 0.4 mm AP for arm structure and 1.4 mm ± 0.2 mm LR, 1.1 ± 0.1 mm SI, and 0.2 ± 0.0 mm AP for shoulder structure. For rotational errors in each axis, 2.1°, 1.2°, 0.9° for arm structure and 0.2°, 0.4°, 1.5° for shoulder structure.

Figure 25 shows an OBI image registered with digitally reconstructed radiography (DRR) image from a planning CT image. When the ROI was set to arm structure, shoulder structures misaligned from the reference position.

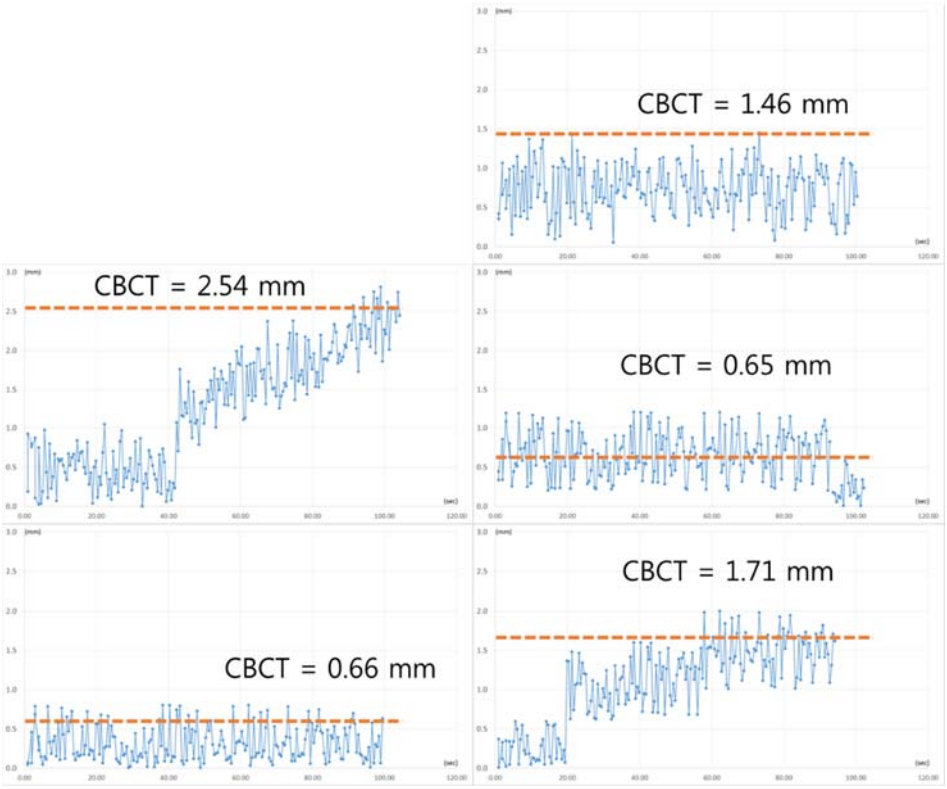

Figure 23. The measured intrafractional motion of Lt inner thigh patient for five fractions. The orange colored horizontal line represents the intrafractional motion estimated from the pre- and post-treatment CBCT images.

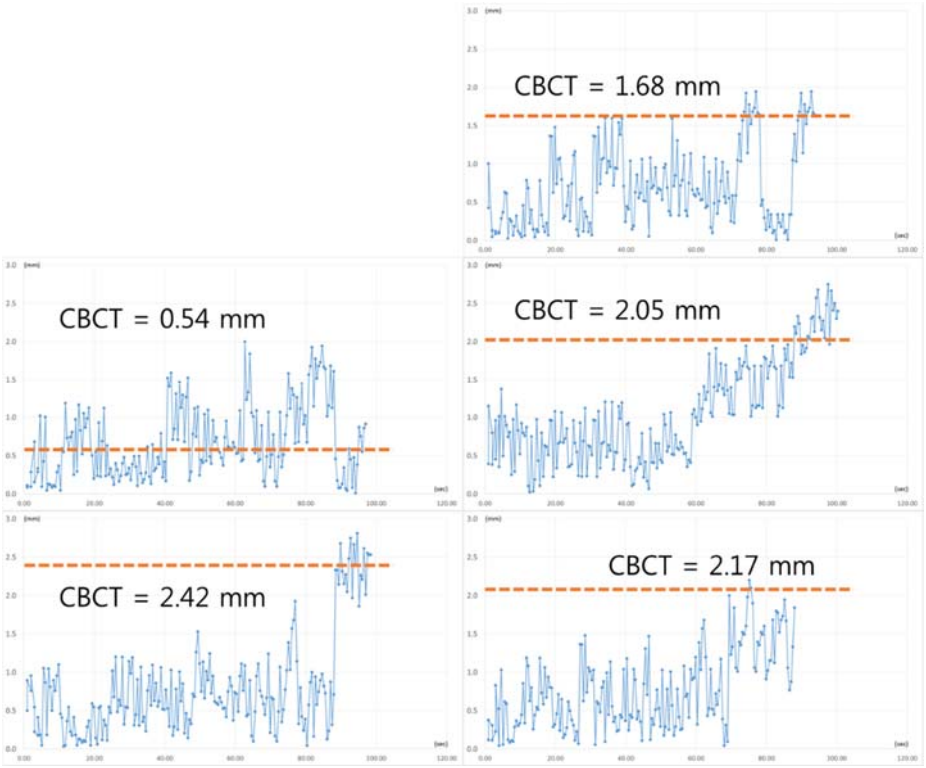

Figure 24. The measured intrafractional motion of Lt knee patient for five fractions. The orange colored horizontal line represents the intrafractional motion estimated from the pre- and post-treatment CBCT images.

TABLE 10. Interfractional errors of each structures observed by ROIM system.

	Arm	Shoulder
Translational (mm)		
LR	3.0 ± 0.6	1.4 ± 0.2
SI	2.7 ± 0.6	1.1 ± 0.1
AP	1.0 ± 0.4	0.2 ± 0.0
Overall	2.2 ± 1.0	0.9 ± 0.5
3D vector	4.1 ± 1.0	1.7 ± 0.2
Rotational (°)		
Pitch	2.1	0.2
Yaw	1.2	0.4
Roll	0.9	1.5

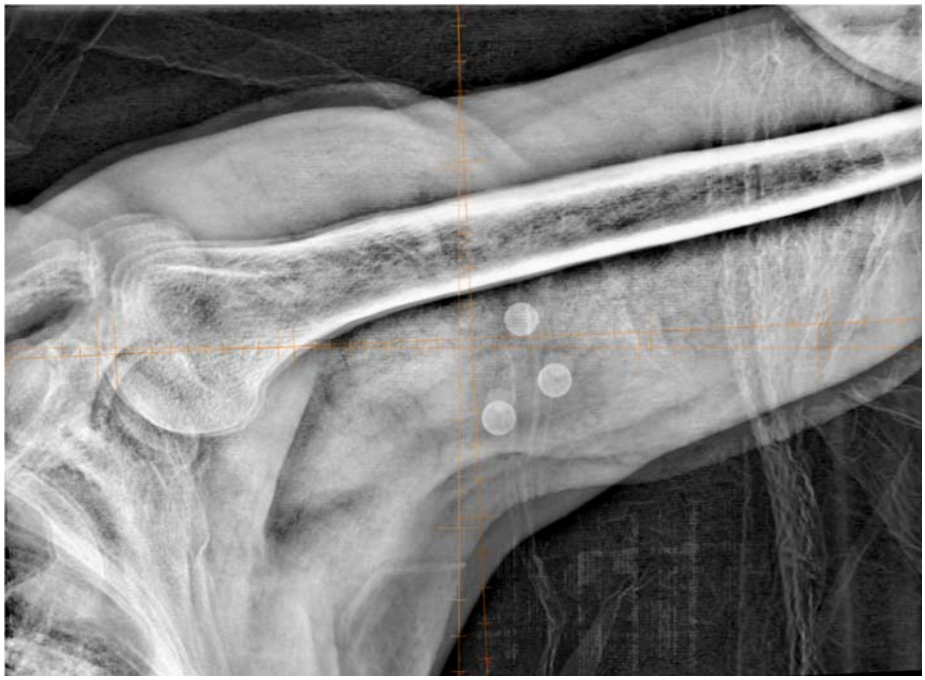

Figure 25. An OBI image registered with digitally reconstructed radiography (DRR) image from a planning CT image. When the ROI was set to arm structure, shoulder structures misaligned from the reference position.

3.B.c. Comparison

The derived MAE and SD of MIs were 0.83 ± 0.12, 0.89 ± 0.20, 0.88 ± 0.32, and 0.91 ± 0.22 for $CBCT_{w/o\ rot}$, $CBCT_{w/\ rot}$, $ROIM_{w/o\ rot}$, and $ROIM_{w/\ rot}$, respectively. Higher MI implies better localization of the patient. This indicates that motion correction with the ROIM system is equivalent or superior than the CBCT based method. The corrected image with respect to the setup errors derived from the CBCT rigid body registration showed that the bony landmarks were perfectly matched, however, the surface and soft tissue region were not. In contrast, the corrected image with respect to the setup errors derived from ROIM system showed that the surface and soft tissue region including PTV were well aligned with the reference planning CT image.

Figure 26 and Figure 27 shows a comparison of correction result with respect to the derived setup errors by CBCT vs. ROIM. The corrected image with respect to the setup errors derived from the CBCT rigid body registration with only translational correction showed that the bony landmarks were perfectly matched, however, the surface and soft tissue region were not matched well. In contrast, the corrected image with respect to the setup errors derived from ROIM system showed that the surface and soft tissue region including PTV were matched well with the reference planning CT image.

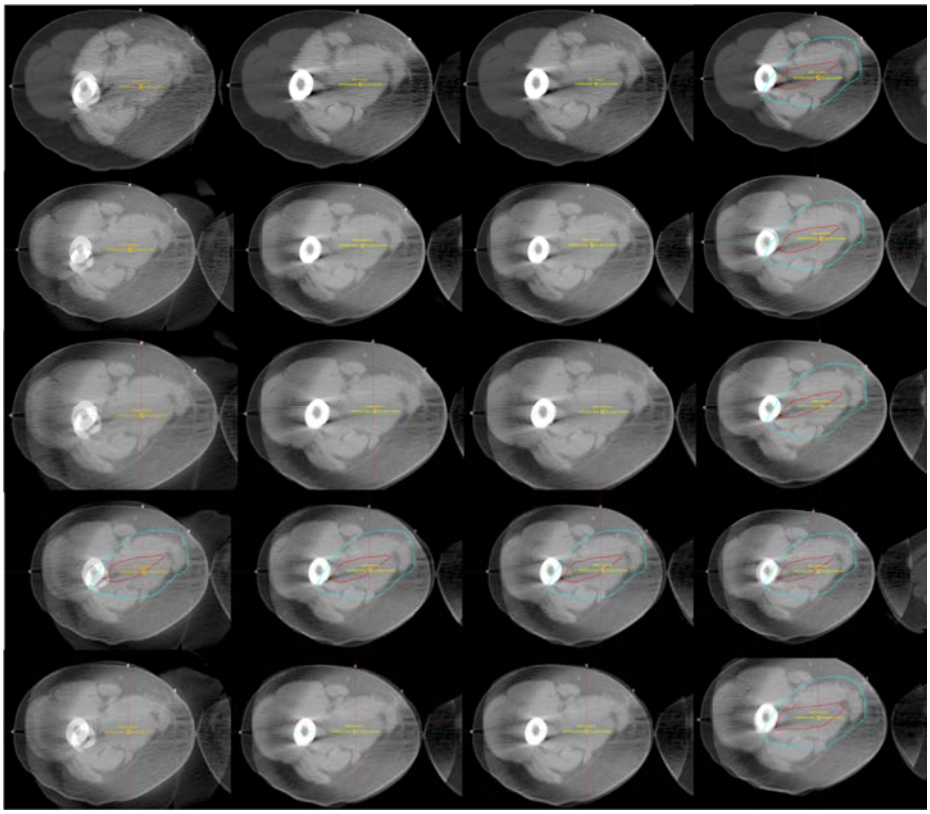

Figure 26. A comparison of correction result with respect to the derived setup errors by CBCT vs. ROIM for Lt. inner thigh patient.

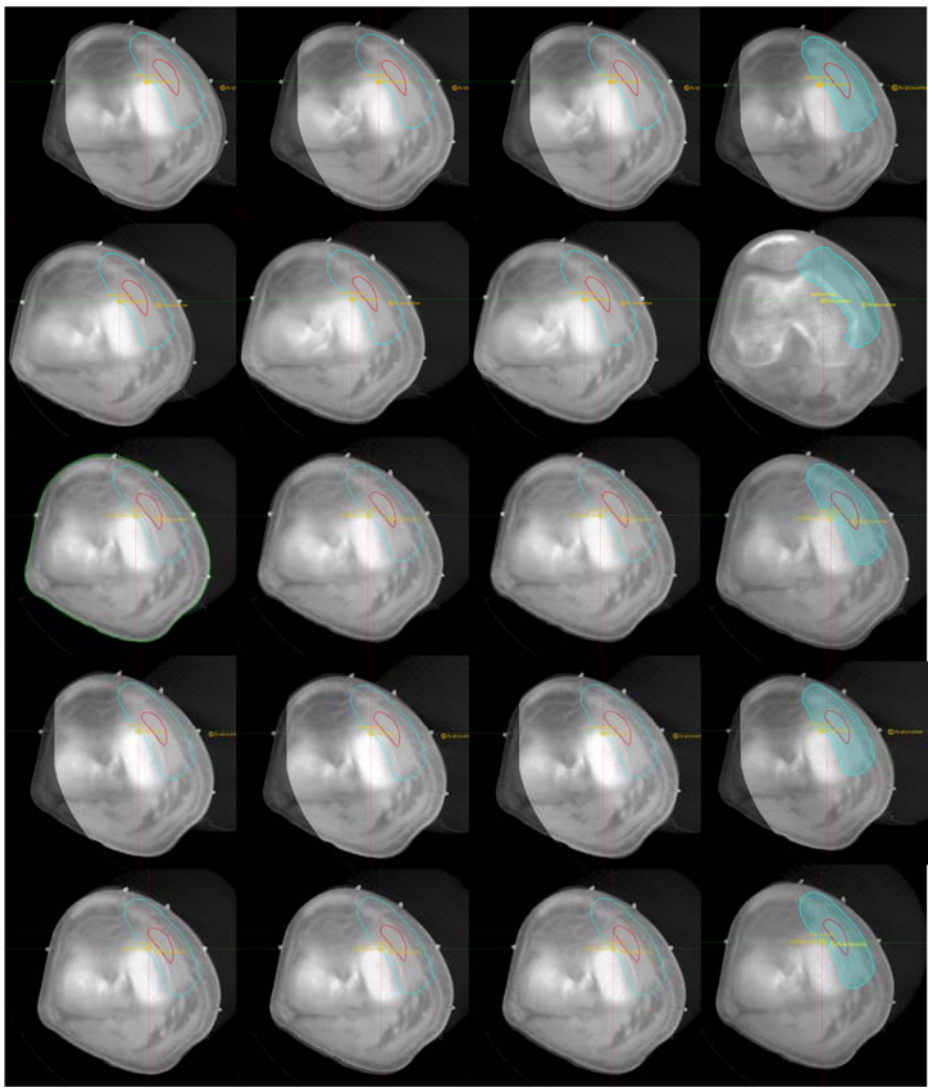

Figure 27. A comparison of correction result with respect to the derived setup errors by CBCT vs. ROIM for Lt. knee patient.

4. Discussions

Direct visualization of the extremities region or bony landmarks using EPID and kV radiographs provides reasonable accuracy, but is not acceptable when all 6 DOF are considered [76]. Six DOF registration of optical images with the planned CT images provides a more complete evaluation of positioning accuracy than 3D registration used in conventional methods [77, 78].

Zhu *et al*. showed that the CBCT system can also detect translation and rotation of a phantom with accuracies of 1 mm and 0.2°, respectively. However, offsets less than 1 mm translation and 0.2° rotation were not detectable [79]. X-ray based guidance with the ExacTrac® system provides monitoring of 3D quantitative rotational and translational errors. Chang *et al.* showed general agreement between the ExacTrac® system and CBCT [80]. However, daily use of these systems may result in excessive radiation exposure. An optical image guided system would reduce potential radiation dose.

Kim *et al.* showed that the marker matching algorithm of the ExacTrac® system yielded 3D uncertainty of 0.30 ± 0.40 mm [51]. In comparison, the proposed ROIM system had accuracy 0.50 ± 0.67 mm for a head phantom by directly detecting IR markers, even with the immobilization device. This relatively large uncertainty compared to the ExacTrac® system was caused by detecting IR markers behind a thermoplastic mold. However, ROIM is still feasible for correcting the daily setup for extremity patients within sub-millimeter accuracy [42]. The system can derive localization corrections from 6 DOF registration of the IR markers with the reference setup.

Hass *et al.* showed that daily image guidance is essential to determine

comprehensive PTV margins for extremity STS patients [53]. Optical based systems offer non-invasive and real time image guidance [81], and so are more suitable for daily image guidance than X-ray based systems. Commercial optical based systems (e.g. AlignRT®, frameless SonArray™, and ExacTrac®) are available, but system accuracy strongly depends on the selected ROI for surface reconstruction [82]. Although the thermoplastic mold would be an option for effective limb immobilization, the device should be modified to allow patient surface capture using these systems [82–84].

The proposed ROIM optical based guidance system detects IR markers even behind the thermoplastic mold [81]. In addition to accurate assessment of geometrical uncertainties in radiotherapy, the ROIM system is more efficient and flexible than existing commercial offerings, and promotes expanded clinical usage.

Dickie *et al.* studied motion monitoring results through CBCT and an optical localization system (OLS) in pre-operative intensity modulated radiation therapy (IMRT) subjects [63]. The study comprehensively addressed PTV margin for lower extremity STS patients. We believe the current study is the first clinical implementation of real time optical image-guided RT established on post-operative 3D-CRT candidates including upper extremity cases.

In this study, the proposed ROIM system was developed and applied in clinical practice. ROIM offers auxiliary or alternative patient monitoring to X-ray based systems.

(a) Compared to intra-abdominal lesions, extremities have less or no deformation of the internal organs during a single fraction. Thus, monitoring with optical image based system using external fiducial markers is sufficient.

(b) Rotational motions derived by CBCT registration with the planned CT image were not consistent with those observed from ROIM system. Quantitative comparison using MI showed the ROIM system was the more accurate monitoring system in terms of soft tissue alignment.

(c) Real time motion monitoring of extremity STS patients was feasible during treatment. ROIM also showed utility in patient setup, including rotational correction.

(d) ROIM monitors 3D patient motion even when CBCT volumetric imaging was not possible due to large couch shift, which is common in this patient population.

(e) ROIM provides feasible multiple ROI motion assessment, as particularly demonstrated in the case of patient 5. In contrast, CBCT only provides for rigid body registration of the whole CBCT image.

One limitation of this study was that optical image based monitoring was not possible for patients whose treatment plan included bolus compensation, because IR markers could not be attached.

ROIM cannot offer direct monitoring of internal motion. Thus, the system

can only be applied to a limited patient population (e.g. extremity, H&N). X-ray based monitoring is necessary to compensate for inter-fractional deformation of internal geometry, if it occurs.

Dickie *et al.*, clinically implemented comprehensive PTV margins using the population based formula recommended by van Herk *et al.* [63,85]. However, we could not calculate this margin because of the small sample size to derive systematic and random errors.

The vacuum cradle did not offer consistent setup for extremity STS patients. Engelsman *et al.*, stated that rigid immobilization devices tend to offer more consistent patient positioning than non-rigid devices, such as vacuum cradles [86]. Thus, more rigorous and individual immobilization methods are required for this patient population.

5. Conclusions

We demonstrated clinical feasibility of the in-house ROIM system to monitor daily extremity STS patient's motion in real time with acceptable accuracy and precision. ROIM can be used as an auxiliary or alternative means of daily image guided RT, particularly because daily and real-time CBCT scanning is not suitable for this patient population.

GENERAL DISCUSSION

The proposed system consists of two individual systems to assess geometrical uncertainties in radiotherapy. AutoMQA provides assessment of machine related errors and ROIM assesses patient related errors. Prior to treatment, LINAC mechanical properties should be guaranteed consistent with the desired values set during the planning stage.

AutoMQA has strong potential for application of IMRT or VMAT QA. If we apply AutoMQA clinically, we can believe the reported machine parameters prior to each treatment session, and only patient related errors need operator attention.

Assessment of patient related errors is currently imperfect, but worth of addressing because patient life quality could be greatly improved if treatment volume localization was better controlled. The proposed ROIM system is optical image based, so internal treatment volume motion cannot be assessed. However, ROIM is real time motion tracking and can detect excessive movement of the treatment region with external surrogates. Patient localization could be significantly improved by 6 DOF correction using the ROIM system.

AutoMQA would need to be modified to enable assessment of machine related errors during treatment sessions. Real time synchronization with machine parameters provided by the LINAC itself, and additional image processing module(s) for multi leaf collimator (MLC) movement assessment

are required. With these modifications, real time assessment of overall geometrical uncertainties during the treatment session is feasible.

In addition to providing accurate assessment of geometrical uncertainties in radiotherapy, the developed systems have more efficiency and flexibility for expanding RT usage in our busy clinic than other commercial systems.

CONCLUSIONS

The proposed AutoMQA and ROIM systems can effectively assess machine and patient geometric uncertainties in radiotherapy, respectively. The combined system has strong potential for clinical application to improve radiotherapy precision.

REFERENCES

[1]C. F. Hess, R. D. Kortmann, R. Jany, A. Hamberger and M. Bamberg, "Accuracy of field alignment in radiotherapy of head and neck cancer utilizing individualized face mask immobilization: a retrospective analysis of clinical practice," Radiother. Oncol. **34**, 69-72 (1995).

[2]J. A. Purdy, "Future directions in 3-D treatment planning and delivery: a physicist's perspective," Int. J. Radiat. Oncol. Biol. Phys. **46**, 3-6 (2000).

[3]J. Boda-Heggemann, C. Walter, A. Rahn, H. Wertz, I. Loeb, F. Lohr and F. Wenz, "Repositioning accuracy of two different mask systems-3D revisited: comparison using true 3D/3D matching with cone-beam CT," Int. J. Radiat. Oncol. Biol. Phys. **66**, 1568-1575 (2006).

[4]B. C. Cho, M. van Herk, B. J. Mijnheer and H. Bartelink, "The effect of set-up uncertainties, contour changes, and tissue inhomogeneities on target dose-volume histograms," Med. Phys. **29**, 2305-2318 (2002).

[5]M. van Herk, P. Remeijer, C. Rasch and J. V. Lebesque, "The probability of correct target dosage: dose-population histograms for deriving treatment margins in radiotherapy," Int. J. Radiat. Oncol. Biol. Phys. **47**, 1121-1135 (2000).

[6]L. Xing, Z. Lin, S. S. Donaldson, Q. T. Le, D. Tate, D. R. Goffinet, S. Wolden, L. Ma and A. L. Boyer, "Dosimetric effects of patient displacement and collimator and gantry angle misalignment on intensity modulated radiation therapy," Radiother. Oncol. **56**, 97-108 (2000).

[7]E. E. Klein, J. Hanley, J. Bayouth, F. F. Yin, W. Simon, S. Dresser, C. Serago, F. Aguirre, L. Ma, B. Arjomandy, C. Liu, C. Sandin, T. Holmes and A. A. o. P. i. M. Task Group, "Task Group 142 report: quality assurance of medical accelerators," Med. Phys. **36**, 4197-4212 (2009).

[8]B. Poppe, P. Mehran, R. Kollhoff and A. Rubach, "Use of a two-dimensional ionization chamber array for quality assurance in medical linear accelerators," Zeitschrift fur medizinische Physik **13**, 115-122 (2003).

[9]K. T. Welsh, L. E. Reinstein and R. A. Wlodarczyk, "Automated image based quality assurance for medical linear accelerators," in *The Use of Computers in Radiation Therapy,* (Springer, 2000), pp. 368-370.

[10]P. Winkler, H. Bergmann, G. Stuecklschweiger and H. Guss, "Introducing a system for automated control of rotation axes, collimator and laser adjustment for a medical linear accelerator," Phys. Med. Biol. **48**, 1123-1132 (2003).

[11]B. Casar, D. Cugura, I. M. Carot, I. Vojvodic and S. Rebersek, presented at the World Congress on Medical Physics and Biomedical Engineering, September 7-12, 2009, Munich, Germany, 2009 (unpublished).

[12]M. J. Nyflot, N. Cao, J. Meyer and E. C. Ford, "Improved accuracy for noncoplanar radiotherapy: an EPID-based method for submillimeter alignment of linear accelerator table rotation with MV isocenter," J. Appl. Clin. Med. Phys. **15**, 4682 (2014).

[13]W. Du and J. Yang, "A robust Hough transform algorithm for determining the radiation centers of circular and rectangular fields with subpixel accuracy," Phys. Med. Biol. **54**, 555-567 (2009).

[14]J. Adamson and Q. Wu, "Independent verification of gantry angle for pre-treatment VMAT QA using EPID," Phys. Med. Biol. **57**, 6587-6600 (2012).

[15]B. Arjomandy and M. D. Altschuler, "A quality assurance device for the accuracy of the isocentres of teletherapy and simulation machines," Phys. Med. Biol. **45**,

2207-2217 (2000).
[16]P. Rowshanfarzad, C. K. McGarry, M. P. Barnes, M. Sabet and M. A. Ebert, "An EPID-based method for comprehensive verification of gantry, EPID and the MLC carriage positional accuracy in Varian linacs during arc treatments," Radiat. Oncol. **9**, 249 (2014).
[17]P. Rowshanfarzad, M. Sabet, M. P. Barnes, D. J. O'Connor and P. B. Greer, "EPID-based verification of the MLC performance for dynamic IMRT and VMAT," Med. Phys. **39**, 6192-6207 (2012).
[18]P. Rowshanfarzad, M. Sabet, D. J. O'Connor, P. M. McCowan, B. M. McCurdy and P. B. Greer, "Detection and correction for EPID and gantry sag during arc delivery using cine EPID imaging," Med. Phys. **39**, 623-635 (2012).
[19]D. A. Low, J. F. Dempsey, J. Markman, S. Mutic, E. E. Klein, J. W. Sohn and J. A. Purdy, "Toward automated quality assurance for intensity- modulated radiation therapy," Int. J. Radiat. Oncol. Biol. Phys. **53**, 443-452 (2002).
[20]J. G. Li, J. F. Dempsey, L. Ding, C. Liu and J. R. Palta, "Validation of dynamic MLC-controller log files using a two-dimensional diode array," Med. Phys. **30**, 799-805 (2003).
[21]K. T. Welsh, R. A. Wlodarczyk and L. E. Reinstein, "A new geometric and mechanical verification device for medical LINACs," J. Appl. Clin. Med. Phys. **3**, 154-161 (2002).
[22]S. D. Burdette, T. E. Herchline and R. Oehler, "Surfing the web: practicing medicine in a technological age: using smartphones in clinical practice," Clinical infectious diseases : an official publication of the Infectious Diseases Society of America **47**, 117-122 (2008).
[23]M. Hussain, A. Al-Haiqi, A. A. Zaidan, B. B. Zaidan, M. L. Kiah, N. B. Anuar and M. Abdulnabi, "The landscape of research on smartphone medical apps: Coherent taxonomy, motivations, open challenges and recommendations," Computer methods and programs in biomedicine **122**, 393-408 (2015).
[24]B. Martinez-Perez, I. de la Torre-Diez, M. Lopez-Coronado, B. Sainz-de-Abajo, M. Robles and J. M. Garcia-Gomez, "Mobile clinical decision support systems and applications: a literature and commercial review," Journal of medical systems **38**, 4 (2014).
[25]I. de la Torre-Diez, B. Martinez-Perez, M. Lopez-Coronado, J. R. Diaz and M. M. Lopez, "Decision support systems and applications in ophthalmology: literature and commercial review focused on mobile apps," Journal of medical systems **39**, 174 (2015).
[26]Y. Tian, T. S. Zhou, Q. Yao, M. Zhang and J. S. Li, "Use of an agent-based simulation model to evaluate a mobile-based system for supporting emergency evacuation decision making," Journal of medical systems **38**, 149 (2014).
[27]V. Chandrasekaran, R. Dantu, S. Jonnada, S. Thiyagaraja and K. P. Subbu, "Cuffless Differential Blood Pressure Estimation Using Smart Phones," Ieee T Bio-Med Eng **60**, 1080-1089 (2013).
[28]D. D. McManus, J. Lee, O. Maitas, N. Esa, R. Pidikiti, A. Carlucci, J. Harrington, E. Mick and K. H. Chon, "A novel application for the detection of an irregular pulse using an iPhone 4S in patients with atrial fibrillation," Heart Rhythm **10**, 315-319 (2013).
[29]G. L. Warnock, "The use of apps in surgery," Can J Surg **55**, 77-77 (2012).
[30]S. Ayub, A. Bahraminisaab and B. Honary, presented at the Proceedings of the 13th Annual Post Graduate Symposium on the Convergence of Telecommunications, Networking and Broadcasting, Liverpool, 2012

(unpublished).
[31]K. Maenaka, presented at the Networked Sensing Systems, 2008. INSS 2008. 5th International Conference on Networked Sensing Systems, 2008 (unpublished).
[32]D. Gebre-Egziabher, R. C. Hayward and J. D. Powell, "Design of multi-sensor attitude determination systems," IEEE Transactions on Aerospace and Electronic Systems **40**, 627-649 (2004).
[33]M. Roushdy, "Detecting coins with different radii based on hough transform in noisy and deformed image," GVIP Journal **7**, 25-29 (2007).
[34]C. Harris and M. Stephens, presented at the Alvey vision conference, 1988 (unpublished).
[35]T. Ono, H. Takegawa, T. Ageishi, M. Takashina, H. Numasaki, M. Matsumoto and T. Teshima, "Respiratory monitoring with an acceleration sensor," Phys. Med. Biol. **56**, 6279-6289 (2011).
[36]H. Schiefer, N. Ingulfsen, J. Kluckert, S. Peters and L. Plasswilm, "Measurements of isocenter path characteristics of the gantry rotation axis with a smartphone application," Med. Phys. **42**, 1184-1192 (2015).
[37]S. L. Meeks, J. M. Buatti, F. J. Bova, W. A. Friedman, W. M. Mendenhall and R. A. Zlotecki, "Potential clinical efficacy of intensity-modulated conformal therapy," Int. J. Radiat. Oncol. Biol. Phys. **40**, 483-495 (1998).
[38]C. P. Karger, O. Jakel, J. Debus, S. Kuhn and G. H. Hartmann, "Three-dimensional accuracy and interfractional reproducibility of patient fixation and positioning using a stereotactic head mask system," Int. J. Radiat. Oncol. Biol. Phys. **49**, 1493-1504 (2001).
[39]S. Li, D. Liu, G. Yin, P. Zhuang and J. Geng, "Real-time 3D-surface-guided head refixation useful for fractionated stereotactic radiotherapy," Med. Phys. **33**, 492 (2006).
[40]A. W. Lightstone, S. H. Benedict, F. J. Bova, T. D. Solberg and R. L. Stern, "Intracranial stereotactic positioning systems: Report of the American Association of Physicists in Medicine Radiation Therapy Committee Task Group no. 68," Med. Phys. **32**, 2380-2398 (2005).
[41]T. S. Hong, W. A. Tome, R. J. Chappell, P. Chinnaiyan, M. P. Mehta and P. M. Harari, "The impact of daily setup variations on head-and-neck intensity-modulated radiation therapy," Int. J. Radiat. Oncol. Biol. Phys. **61**, 779-788 (2005).
[42]S. Li, D. Liu, G. Yin, P. Zhuang and J. Geng, "Real-time 3D-surface-guided head refixation useful for fractionated stereotactic radiotherapy," Med Phys **33**, 492-503 (2006).
[43]F. J. Bova, J. M. Buatti, W. A. Friedman, W. M. Mendenhall, C. C. Yang and C. Liu, "The University of Florida frameless high-precision stereotactic radiotherapy system," Int. J. Radiat. Oncol. Biol. Phys. **38**, 875-882 (1997).
[44]J. M. Buatti, F. J. Bova, W. A. Friedman, S. L. Meeks, R. B. Marcus, Jr., J. P. Mickle, T. L. Ellis and W. M. Mendenhall, "Preliminary experience with frameless stereotactic radiotherapy," Int. J. Radiat. Oncol. Biol. Phys. **42**, 591-599 (1998).
[45]T. H. Wagner, S. L. Meeks, F. J. Bova, W. A. Friedman, T. R. Willoughby, P. A. Kupelian and W. Tome, "Optical tracking technology in stereotactic radiation therapy," Med. Dosim. **32**, 111-120 (2007).
[46]C. Bert, K. G. Metheany, K. Doppke and G. T. Chen, "A phantom evaluation of a stereo-vision surface imaging system for radiotherapy patient setup," Med Phys **32**, 2753-2762 (2005).
[47]P. J. Schoffel, W. Harms, G. Sroka-Perez, W. Schlegel and C. P. Karger, "Accuracy of

a commercial optical 3D surface imaging system for realignment of patients for radiotherapy of the thorax," Phys. Med. Biol. **52**, 3949-3963 (2007).

[48]J. L. Peng, D. Kahler, J. G. Li, S. Samant, G. Yan, R. Amdur and C. Liu, "Characterization of a real-time surface image-guided stereotactic positioning system," Med Phys **37**, 5421-5433 (2010).

[49]N. Linthout, D. Verellen, K. Tournel and G. Storme, "Six dimensional analysis with daily stereoscopic x-ray imaging of intrafraction patient motion in head and neck treatments using five points fixation masks," Med Phys **33**, 504-513 (2006).

[50]N. Ramakrishna, F. Rosca, S. Friesen, E. Tezcanli, P. Zygmanszki and F. Hacker, "A clinical comparison of patient setup and intra-fraction motion using frame-based radiosurgery versus a frameless image-guided radiosurgery system for intracranial lesions," Radiother. Oncol. **95**, 109-115 (2010).

[51]S. Kim, H. C. Akpati, J. E. Kielbasa, J. G. Li, C. R. Liu, R. J. Amdur and J. R. Palta, "Evaluation of intrafraction patient movement for CNS and head & neck IMRT," Med. Phys. **31**, 500-506 (2004).

[52]B. O'Sullivan, A. M. Griffin, C. I. Dickie, M. B. Sharpe, P. W. Chung, C. N. Catton, P. C. Ferguson, J. S. Wunder, B. M. Deheshi, L. M. White, R. A. Kandel, D. A. Jaffray and R. S. Bell, "Phase 2 study of preoperative image-guided intensity-modulated radiation therapy to reduce wound and combined modality morbidities in lower extremity soft tissue sarcoma," Cancer **119**, 1878-1884 (2013).

[53]R. L. Haas, T. F. Delaney, B. O'Sullivan, R. B. Keus, C. Le Pechoux, P. Olmi, J. P. Poulsen, B. Seddon and D. Wang, "Radiotherapy for management of extremity soft tissue sarcomas: why, when, and where?," Int. J. Radiat. Oncol. Biol. Phys. **84**, 572-580 (2012).

[54]J. M. Felderhof, C. L. Creutzberg, H. Putter, R. A. Nout, J. V. Bovee, P. D. Dijkstra, H. H. Hartgrink and C. A. Marijnen, "Long-term clinical outcome of patients with soft tissue sarcomas treated with limb-sparing surgery and postoperative radiotherapy," Acta Oncol. **52**, 745-752 (2013).

[55]J. E. Tepper and H. D. Suit, "The role of radiation therapy in the treatment of sarcoma of soft tissue," Cancer Invest. **3**, 587-592 (1985).

[56]H. D. Suit, H. J. Mankin, W. C. Wood and K. H. Proppe, "Preoperative, intraoperative, and postoperative radiation in the treatment of primary soft tissue sarcoma," Cancer **55**, 2659-2667 (1985).

[57]J. Lee, Y. J. Park, D. S. Yang, W. S. Yoon, J. A. Lee, C. H. Rim and C. Y. Kim, "Treatment outcome of conservative surgery plus postoperative radiotherapy for extremity soft tissue sarcoma," Radiation oncology journal **30**, 62-69 (2012).

[58]A. M. Davis, B. O'Sullivan, R. Turcotte, R. Bell, C. Catton, P. Chabot, J. Wunder, A. Hammond, V. Benk, R. Kandel, K. Goddard, C. Freeman, A. Sadura, B. Zee, A. Day, D. Tu, J. Pater, G. Canadian Sarcoma and N. C. I. C. C. T. G. R. Trial, "Late radiation morbidity following randomization to preoperative versus postoperative radiotherapy in extremity soft tissue sarcoma," Radiother. Oncol. **75**, 48-53 (2005).

[59]C. I. Dickie, A. M. Griffin, A. L. Parent, P. W. Chung, C. N. Catton, J. Svensson, P. C. Ferguson, J. S. Wunder, R. S. Bell, M. B. Sharpe and B. O'Sullivan, "The relationship between local recurrence and radiotherapy treatment volume for soft tissue sarcomas treated with external beam radiotherapy and function preservation surgery," Int. J. Radiat. Oncol. Biol. Phys. **82**, 1528-1534 (2012).

[60]D. Wang, Q. Zhang, B. L. Eisenberg, J. M. Kane, X. A. Li, D. Lucas, I. A. Petersen, T. F. DeLaney, C. R. Freeman, S. E. Finkelstein, Y. J. Hitchcock, M. Bedi, A. K. Singh, G. Dundas and D. G. Kirsch, "Significant Reduction of Late Toxicities in Patients With Extremity Sarcoma Treated With Image-Guided Radiation Therapy to a Reduced Target Volume: Results of Radiation Therapy Oncology Group RTOG-0630 Trial," J. Clin. Oncol. **33**, 2231-2238 (2015).

[61]J. C. Stroom and B. J. Heijmen, "Limitations of the planning organ at risk volume (PRV) concept," Int. J. Radiat. Oncol. Biol. Phys. **66**, 279-286 (2006).

[62]C. I. Dickie, A. Parent, A. Griffin, T. Craig, C. Catton, P. Chung, T. Panzarella, B. O'Sullivan and M. Sharpe, "A device and procedure for immobilization of patients receiving limb-preserving radiotherapy for soft tissue sarcoma," Med. Dosim. **34**, 243-249 (2009).

[63]C. I. Dickie, A. L. Parent, P. W. Chung, C. N. Catton, T. Craig, A. M. Griffin, T. Panzarella, P. C. Ferguson, J. S. Wunder, R. S. Bell, M. B. Sharpe and B. O'Sullivan, "Measuring interfractional and intrafractional motion with cone beam computed tomography and an optical localization system for lower extremity soft tissue sarcoma patients treated with preoperative intensity-modulated radiation therapy," Int. J. Radiat. Oncol. Biol. Phys. **78**, 1437-1444 (2010).

[64]G. X. Ding and C. W. Coffey, "Radiation dose from kilovoltage cone beam computed tomography in an image-guided radiotherapy procedure," Int. J. Radiat. Oncol. Biol. Phys. **73**, 610-617 (2009).

[65]P. J. Keall, J. A. Ng, P. Juneja, R. T. O'Brien, C. Y. Huang, E. Colvill, V. Caillet, E. Simpson, P. R. Poulsen, A. Kneebone, T. Eade and J. T. Booth, "Real-Time 3D Image Guidance Using a Standard LINAC: Measured Motion, Accuracy, and Precision of the First Prospective Clinical Trial of Kilovoltage Intrafraction Monitoring-Guided Gating for Prostate Cancer Radiation Therapy," Int. J. Radiat. Oncol. Biol. Phys. **94**, 1015-1021 (2016).

[66]J. Y. Weng, P. Cohen and M. Herniou, "Camera Calibration with Distortion Models and Accuracy Evaluation," Ieee Transactions on Pattern Analysis and Machine Intelligence **14**, 965-980 (1992).

[67]Z. Y. Zhang, "A flexible new technique for camera calibration," Ieee Transactions on Pattern Analysis and Machine Intelligence **22**, 1330-1334 (2000).

[68]Z. Y. Zhang, D. Y. Zhu, J. Zhang and Z. M. Peng, "Improved robust and accurate camera calibration method used for machine vision application," Optical Engineering **47**, - (2008).

[69]H. Hatze, "High-Precision 3-Dimensional Photogrammetric Calibration and Object Space Reconstruction Using a Modified Dlt-Approach," Journal of Biomechanics **21**, 533-538 (1988).

[70]H. C. Longuethiggins, "A Computer Algorithm for Reconstructing a Scene from 2 Projections," Nature **293**, 133-135 (1981).

[71]P. Bao, L. Zhang and X. Wu, "Canny edge detection enhancement by scale multiplication," IEEE transactions on pattern analysis and machine intelligence **27**, 1485-1490 (2005).

[72]B. Jian and B. C. Vemuri, "A Robust Algorithm for Point Set Registration Using Mixture of Gaussians," Proceedings / IEEE International Conference on Computer Vision. IEEE International Conference on Computer Vision **2**, 1246-1251 (2005).

[73]L. Zhang, A. S. Garden, J. Lo, K. K. Ang, A. Ahamad, W. H. Morrison, D. I. Rosenthal, M. S. Chambers, X. R. Zhu, R. Mohan and L. Dong, "Multiple

regions-of-interest analysis of setup uncertainties for head-and-neck cancer radiotherapy," Int. J. Radiat. Oncol. Biol. Phys. **64**, 1559-1569 (2006).

[74]P. Viola and W. M. Wells, "Alignment by maximization of mutual information," Int J Comput Vision **24**, 137-154 (1997).

[75]F. Maes, A. Collignon, D. Vandermeulen, G. Marchal and P. Suetens, "Multimodality image registration by maximization of mutual information," IEEE Trans. Med. Imaging **16**, 187-198 (1997).

[76]J. M. Balter, K. L. Lam, H. M. Sandler, J. F. Littles, R. L. Bree and R. K. Ten Haken, "Automated localization of the prostate at the time of treatment using implanted radiopaque markers: technical feasibility," Int. J. Radiat. Oncol. Biol. Phys. **33**, 1281-1286 (1995).

[77]R. D. Kortmann, C. F. Hess, R. Jany, C. Meisner and M. Bamberg, "Reproducibility of field alignment in difficult patient positioning," Int. J. Radiat. Oncol. Biol. Phys. **29**, 869-872 (1994).

[78]R. D. Kortmann, C. F. Hess, W. Hoffmann, R. Jany and M. Bamberg, "Is the standardized helmet technique adequate for irradiation of the brain and the cranial meninges?," Int. J. Radiat. Oncol. Biol. Phys. **32**, 241-244 (1995).

[79]J. Zhu, "Feasibility of using cone-beam CT to verify and reposition the optically guided target localization of linear accelerator based stereotactic radiosurgery," Med Phys **38**, 390-396 (2011).

[80]J. Ma, Z. Chang, Z. Wang, Q. Jackie Wu, J. P. Kirkpatrick and F. F. Yin, "ExacTrac X-ray 6 degree-of-freedom image-guidance for intracranial non-invasive stereotactic radiotherapy: comparison with kilo-voltage cone-beam CT," Radiother. Oncol. **93**, 602-608 (2009).

[81]H. Kim, Y.-K. Park, I. H. Kim, K. Lee and S.-J. Ye, "Development of an optical-based image guidance system: Technique detecting external markers behind a full facemask," Med. Phys. **38**, 3006 (2011).

[82]J. L. Peng, D. Kahler, J. G. Li, S. Samant, G. Yan, R. Amdur and C. Liu, "Characterization of a real-time surface image-guided stereotactic positioning system," Med. Phys. **37**, 5421 (2010).

[83]N. Linthout, D. Verellen, K. Tournel and G. Storme, "Six dimensional analysis with daily stereoscopic x-ray imaging of intrafraction patient motion in head and neck treatments using five points fixation masks," Med. Phys. **33**, 504 (2006).

[84]S. Kim, H. C. Akpati, J. E. Kielbasa, J. G. Li, C. Liu, R. J. Amdur and J. R. Palta, "Evaluation of intrafraction patient movement for CNS and head & neck IMRT," Med. Phys. **31**, 500 (2004).

[85]M. van Herk, P. Remeijer and J. V. Lebesque, "Inclusion of geometric uncertainties in treatment plan evaluation," Int. J. Radiat. Oncol. Biol. Phys. **52**, 1407-1422 (2002).

[86]M. Engelsman, S. J. Rosenthal, S. L. Michaud, J. A. Adams, R. J. Schneider, S. G. Bradley, J. B. Flanz and H. M. Kooy, "Intra- and interfractional patient motion for a variety of immobilization devices," Med. Phys. **32**, 3468-3474 (2005).

Abstract (in Korean)

국 문 초 록

방사선치료는 계획된 빔을 환자의 치료 용적에 정밀하게 전달하는 것을 목표로 하지만 치료 시 의료용 선형가속기나 환자와 관련한 기하학적 불확실성에 의해 이를 보장하기는 쉽지 않다. 이러한 기하학적 불확실성에 의해 환자의 치료 용적이 계획된 처방선량보다 더 작은 선량을 받게 되고 주변의 정상조직에 불필요한 선량을 전달하게 되어 종양제어를 어렵게 하고 합병증의 확률을 높이게 된다. 따라서 환자 치료 시 발생할 수 있는 기하학적 불확실성에 대한 평가와 관리가 필요하다.

본 학위논문의 목적은 의료용 선형가속기와 환자에 관련한 기하학적 불확실성을 평가하기 위한 각각의 시스템을 개발하는 것이다. 첫째로, 의료용 선형가속기에 관련한 기하학적 불확실성을 평가하기 위하여 스마트폰을 이용하여 의료용 선형가속기의 기계적 품질관리를 위한 자동화 시스템을 개발하였다. 둘째로, 환자에 관련한 기하학적 불확실성을 평가하기 위하여 스테레오 카메라를 이용한 광학영상 기반의 환자 움직임 모니터링 시스템을 개발하였다. 각각의 시스템에 대해 정확도와 정밀도를 평가한 후에 실제 임상에 적용하여 그 실용성을 평가하였다.

의료용 선형가속기의 기계적 품질관리를 자동화하기 위한 시스템은 스마트폰에 내장된 모션센서와 고해상도 카메라를

이용하여 구현하였다. 선형가속기 겐트리와 콜리메이터의 회전각도를 평가하기 위하여 모션센서를 이용하였고, 가속기센서와 자이로스코프 등의 센서들의 융합을 통해 중력을 기준으로 한 회전각을 정밀하게 측정 가능하도록 하였다. 치료 조사야의 크기, 십자선의 중심위치, 선원-표면간 거리를 평가하기 위하여 고해상도 카메라로 치료 테이블 위에 투영된 영상을 획득하여 처리하였다.

기계적 품질관리 자동화 시스템의 정확도와 정밀도는 회전각 측정에 대해서는 0.08° ± 0.06°, 그리고 길이 측정에 대해서는 0.42 mm ± 0.27 mm 였다. 본 시스템을 실제 의료용 선형가속기의 기계적 품질관리에 적용하였을 때, 겐트리와 콜리메이터 회전각도 측정의 평균절대오차는 각각 0.08° ± 0.07° 와 0.09° ± 0.07° 였다. 광조사야의 크기, 십자선의 중심위치, 선원-표면간 거리 측정에 대한 평균절대오차는 각각 0.43 mm ± 0.33 mm, 0.51 mm ± 0.22 mm, 그리고 0.79 mm ± 0.25 mm 였다. 본 시스템을 이용하였을 때 위 다섯가지 항목에 대한 기계적 품질관리 시간을 반으로 단축할 수 있었다.

광학영상 기반의 환자 움직임 모니터링 시스템은 두 대의 전하결합소자 카메라로 구성하였다. 본 시스템은 치료실 벽면에 설치되어 의료용 선형가속기의 치료중심을 기준으로 카메라로 촬영된 적외선 반사마커의 3 차원 좌표를 재구성하도록 보정되었다. 기존의 X-선 기반 영상 시스템에 대한 대체적 용도로서 본 시스템의 임상적용 가능성을 평가하기 위하여 5 명의 사지 연부조직 육종환자에 대한 치료간, 치료중의 움직임을 측정하였다.

광학영상 기반의 환자 움직임 모니터링 시스템의 평행이동과 회전 측정의 정확도와 정밀도는 각각 0.3 ± 0.2 mm 와 0.11 ± 0.06° 였다. 본 시스템으로 측정한 환자의 치료간 움직임은 LR 방향으로 2.6 ± 1.4 mm, SI 방향으로 2.8 ± 1.1 mm, 그리고 AP 방향으로 2.0 ± 1.3 mm 였다. 그리고 치료중의 움직임은 LR 방향으로 0.8 ± 1.4 mm, SI 방향으로 0.6 ± 1.1 mm, 그리고 AP 방향으로 0.4 mm ± 0.7 mm 였다.

본 연구로써 개발한 기하학적 불확실성 평가 시스템은 각각 검증된 정확도와 정밀도로 의료용 선형가속기의 기계적 품질관리와 환자의 움직임 평가를 위해 사용될 수 있다. 따라서 본 시스템은 기하학적 불확실성을 평가함으로써 정밀 방사선치료에 기여할 수 있는 가능성을 가진다고 평가할 수 있다.

주요어: 방사선치료, 기하학적 불확실성, 품질보증, 치료간 움직임, 치료내 움직임

학 번: 2010-21892